

용접금속의 충격인성 모델링과
유착 베이나이트의 형성

**Modelling the Impact toughness of
weld metals and
The formation of Coalesced bainite**

**Modelling the Impact toughness of
weld metals and
The formation of Coalesced bainite**

**By
Pak, Jun Hak
Department of Ferrous Technology
(Computational Metallurgy)
Graduate Institute of Ferrous Technology
Pohang University of Science and Technology**

**A thesis submitted to the faculty of Pohang University of
Science and Technology in partial fulfillment of the
requirements for the degree of Master of Science in the
Graduate Institute of Ferrous Technology**

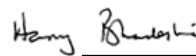
**Pohang, Korea
12. 20. 2007
Approved by**

Prof. Lee, Hae Geon



Major Advisor

Prof. Bhadeshia, H. K. D. H.



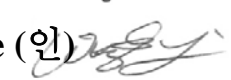
Co-Advisor

용접금속의 충격인성 모델링과 유착 베이나이트의 형성

박 준 학

위 논문은 포항공과대학교 철강대학원 석사학
위 논문으로 학위 논문 심사위원회를 통과하였음을
인정합니다.

2007. 12. 20

학위논문심사위원회	위원장	이 해 건 (인) 
	위원	김 규 영 (인) 
	위원	Qin, Rong Shan (인) 
	위원	Liu, Weijie (인) 

MFT
20062856

박준학 Pak, Jun Hak Modelling the impact toughness of weld metals and The formation of Coalesced bainite, Graduate Institute of Ferrous Technology, 2007, Advisor: Lee, Hae Geon, Co-Advisor: Bhadeshia, H. K. D. H., Text in English

Abstract

The overall aim of this work is to find the way of improving impact toughness of weld metals. There were two kinds of specific work included in the thesis.

One is to find the significant phenomena about impact toughness of weld metal using neural network modelling and to study the related metallurgy. At the beginning of the work, it was discovered that double logarithms used to represent the output form in order to avoid negative outputs leads to unjustified bias in the modelling. The method was therefore abandoned. Through the analysis of neural network predictions, it was found that increasing interpass temperature could reduce impact toughness in some circumstances. It was interesting that unique domains were identified in the nickel-interpass temperature plots, which were not typical in similar plots involving carbon, chromium and manganese.

The later part of the thesis was dedicated to the study of a recent discovery, coalesced bainite, which is known to be detrimental to the toughness of steel. The martensite-start temperatures of the 2Mn and 0.5Mn alloy were systematically measured, followed by the isothermal transformation of samples above the measured martensite-start temperatures. This was done in order to generate the coalesced structure at a constant temperature for the first

time. There seemed to be a greater tendency to form coalesced bainite at low temperatures which is consistent with the qualitative mechanism of the phase. Coalesced bainite was observed not only to originate at austenite grain surfaces but also occurred intragranularly. It has been confirmed that coalesced bainite occurs at the early stages of transformation, which is reasonable given the scale of the phase.

Contents

I . Introduction.....	1
1. Impact toughness of weld metals.....	1
1.1 Impact toughness.....	1
1.2 Welding.....	3
1.3 Variables describing weld metal.....	4
1.3.1 Alloying elements.....	4
1.3.2 Welding parameters.....	5
1.4 Microstructure of weld metal.....	6
2. Neural network.....	6
2.1 Structure of neural network.....	7
2.2 Error estimates.....	8
2.3 Overfitting.....	9
2.4 Significance.....	10
2.5 Committee model.....	11
2.6 An example of application.....	12
3. Coalesced bainite.....	14
3.1 Mechanism.....	14
3.2 Coalesced bainite in weld metals.....	16
II . Experiments.....	17
1. Neural network modelling.....	17
1.1 Collecting data.....	17
1.2 The analysis of database.....	19
2. Coalesced bainite.....	31
2.1 Weld metal.....	31
2.2 Dilatometer.....	31
2.3 Hardness tests.....	32

2.4 Microscopy.....	32
III. Determination of the martensite-start temperature.....	33
1. The transformation-start temperature.....	33
1.1 The 2Mn alloy.....	34
1.2 The 0.5Mn alloy.....	43
2. Discussion about the high $T_S^{y\alpha}$	48
3. Conclusions.....	49
IV. Neural network modelling.....	50
1. Biased models.....	50
2. Interpass temperature.....	54
3. General results of modelling.....	56
4. Results and analyses.....	59
4.1 Effects of individual input variables.....	59
4.2 Influence of interpass temperature.....	64
4.2.1 Manganese.....	65
4.2.2 Carbon and chromium.....	67
4.2.3 Nickel.....	72
5. Discussion.....	75
6. Conclusions.....	78
V. Coalesced bainite.....	79
1. The bainite-start temperature.....	79
2. Coalesced bainite.....	83
2.1 The 2Mn alloy.....	83
2.2 The 0.5Mn alloy.....	88
2.3 Uncertain constituents.....	92
3. Conclusions.....	94
VI. Summary and future works.....	95

VII. References.....	97
Appendix A.....	103
Acknowledgements.....	108
CURRICULUM VITAE.....	110

Nomenclature and Abbreviations

A_{C1}	Temperature at which ferrite starts to transform into austenite during heating (A_C standards for <i>Arret Chauffage</i>)
A_{e1}	Equilibrium temperature for austenite + ferrite or ferrite + cementite phase boundary
D_{Fe}	Variable related with iron diffusion distance during post-weld heat treatment
$ \Delta G^{\gamma\alpha} $	Free energy change for transformation without composition change
M_S	Martensite-start temperature
P	Point source energy input rate
Q	Activation energy
R	Gas constant
r	Polar coordinate with respect to point heat source
T	Temperature
T_0	Temperature at which austenite and ferrite of the same composition have the same free energy

T_0	Far field temperature
$T_S^{\gamma\alpha}$	Transformation temperature austenite to ferrite
T_t	Ductile to brittle transition temperature
$t_{8/5}$	Cooling time between 800 °C and 500 °C
v	Velocity of point heat source
x_n	Normalized value
α	Ferrite
α_a	Acicular ferrite
α_w	Widmanstätten ferrite
κ	Thermal conductivity
ξ	Volume fraction
ξ	coordinate measuring translation of heat source
σ	Standard deviation
BCC	Body-centered cubic

CCT	Continuous cooling transformation
CSLM	Confocal Scanning Laser Microscopy
EBSD	Electron backscatter diffraction
FCC	Face-centered cubic
FEGSEM	Field emission gun scanning electron microscopy
GMAW	Gas metal arc welding
GTAW	Gas-tungsten arc welding
MMAW	Manual metal arc welding
<i>MTDATA</i>	Metallurgical thermochemical databank
HI	Heat input
ISO	International organisation for standardisation
IT	Interpass temperature
ppmw	Parts per million by weight
PWHTT	Post-weld heat treatment temperature
PWHTt	Post-weld heat treatment time

SAW	Submerged arc welding
TEM	Transmission electron microscope
TT	Test temperature for Charpy toughness

I . Introduction

The ultimate aim of this work is to find factors which can improve the impact toughness of weld metals. Thus at first, fundamental information about impact toughness was introduced and then the variables which can affect the toughness were examined. Secondly the basic theory of neural network as a good tool for impact toughness modelling and its application were explained. Finally the qualitative theory of coalesced bainite whose presence was predicted by neural network was also treated.

1. Impact toughness of weld metals

1.1 Impact toughness

Impact toughness is generally represented by a Charpy test in which a square sectioned, notched bar is fractured under given conditions and the energy absorbed in the process is taken as an empirical measure of toughness. The tests are carried over a range of temperature, and a plot of the impact toughness versus temperature is called an impact transition curve, which is usually sigmoidal (Fig. 1.1) (Bhadeshia, 2001).

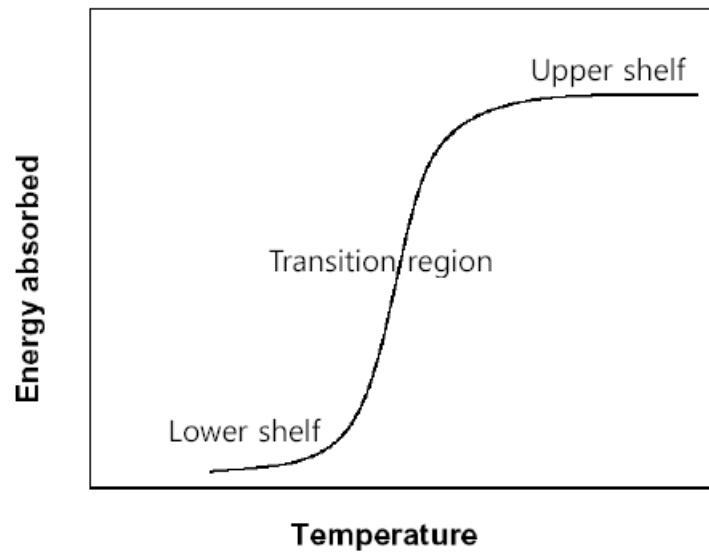


Fig. 1.1: Schematic impact transition curve (Muruganath, 2002)

The flat region of the curve at high temperatures is called the upper shelf and represents ductile failure. The flat region at lower temperatures is called the lower shelf and corresponds cleavage failure. In the transition region between these, cleavage and ductile failure is mixed. The impact transition temperature (T_t) is usually defined as that at which fracture shows 50 % cleavage (Bhadeshia, 2001).

The test is usually performed at a variety of temperatures in order to characterise the ductile to brittle transition intrinsic to body-centered cubic metals. In such metals, the cleavage stress is not sensitive to temperature; on the other hand, the stress required for plastic flow rises rapidly as the temperature decreases (Fig. 1.2). The temperature where the curves representing the cleavage and flow stress cross is represented as the transition temperature (T_t). Below T_t , cleavage is easier than plastic flow and *vice versa* (Bhadeshia, 2001).

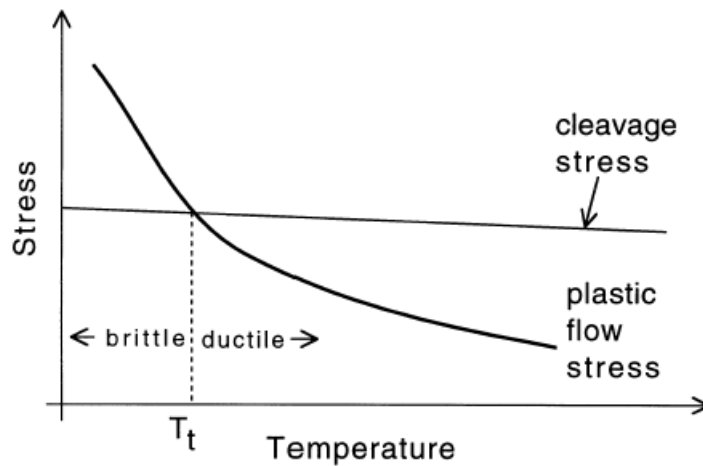


Fig. 1.2: Influence of temperature on the stress required for cleavage and plastic flow (Bhadeshia, 2001)

The Charpy test is empirical in that the data cannot be used directly in material design. It is, nevertheless, an essential quality control measure which is specified widely in international standards, and in the ranking of samples in research and development exercises (Bhadeshia, 2001).

1.2 Welding

Welding is a method for a strong joint between base metals, especially steels. As the field of steel application has enlarged to extreme circumstances, for example, the construction of architectures for oil exploitation in the polar regions such as the North sea and the Gulf of Alaska, higher toughness of weldments have become crucial (Ohkita and Horii, 1995). On the other hand it has been accepted that maintaining good toughness is problematic as strength levels increase above the region of 690 MPa. (Svensson, 1999; Widgery *et al.*, 2002). Improving the impact toughness of weld metals is a challenging issue in metallurgy.

1.3 Variables describing weld metal

To understand weld metals, it is important to know the alloying elements added and the welding parameters.

1.3.1 Alloying elements

Alloying elements are important because they determine microstructural evolution in weld metals. They consequently play a role regarding mechanical properties. Grain refinement by alloying is the most favoured strengthening mechanism in high-strength steel weld metals since it also contributes to toughness. Alloying elements also can cause precipitation strengthening (Keehan, 2004).

Carbon with its strong hardening effect, increases the volume percentage of hard microstructures, *e.g.*, martensite, in a steel weld (Wang 2002).

Manganese and nickel are very important in the solidification process of weld metals. Large additions of these elements can hinder the formation of δ -ferrite entirely and instead the weld metal solidifies directly to austenite (Lord, 1999 and Edvardson *et al.*, 1976). In addition, both elements cause solid solution strengthening.

Silicon contributes to solid solution hardening. The addition of silicon (in high concentrations, 1.5 wt%) have been reported to prevent poor toughness in bainitic steels because it suppresses the precipitation of cementite, which can be brittle (Bhadeshia 1999b). Silicon and manganese are important deoxidising elements in welding systems (Wang 2002).

Nitrogen and oxygen are important solutes which participate in precipitation reaction and in forming non-metallic inclusions that may or may

not be beneficial to the final microstructures and mechanical properties of a weld metal (Wang 2002).

It is important to realize that solute additions to the vast majority of weld metals must be kept at a minimum to avoid the risk of brittle fracture (Bhadeshia, 2007).

1.3.2 Welding parameters

There are five kinds important welding parameters when making electric arc welds: preheating temperature, interpass temperature, heat input, post-weld heat treatment. Since preheat/interpass temperature and heat input influence the cooling rate of the metal, they are important with respect to the final microstructure. Post-weld heat treatment influences the final strength and therefore the toughness. The individual parameters are introduced below.

Preheating refers to the temperature of the base metal, either in its entirety or just the local region surrounding the joint, to a specific desired temperature, called the preheat temperature, prior to welding (Funderburk, 1997).

Interpass temperature is that to which deposited metal is allowed to cool before depositing more metal by welding in a multipass welding (Funderburk, 1998).

Heat input is a relative measure of the energy transferred per unit length of weld during welding. This cannot be measured directly, however, it can be calculated from the measured values of arc voltage, current and welding speed (Funderburk, 1999).

Post-weld heat treatment is defined as any implemented after welding, is

often used to temper microstructure which would otherwise be brittle, or for relieving residual stresses (Funderburk, 1998). Sometimes a low- temperature treatment at 250 °C is used to allow dissolved hydrogen to be removed.

1.4 Microstructure of weld metal

The microstructure of weld metals consists of mixtures of allotriomorphic ferrite (α), Widmanstätten ferrite (α_w), acicular ferrite (α_a) and the so-called microphases, for example, small quantities of retained austenite and martensite (Bhadeshia and Svensson, 1993). Allotriomorphic ferrite is weak and provides easy crack paths and Widmanstätten ferrite suffers from poor toughness because the plates form in parallel packets with few crystallographic discontinuities (Bhadeshia, 2007). On the other hand, acicular ferrite has a very fine grain size and a high concentration of dislocations that are responsible for its good toughness and ductility (Pickering, 1978). Therefore, there have been many attempts to explain the good impact toughness of weld metal in terms of the fraction of acicular ferrite (Ohkita and Horii, 1995). Zhang and Farrar (1997) reported that the best toughness in weld metal was achieved with a high volume fraction of acicular ferrite, although small quantities of other phase are nevertheless desirable. This implied that achieving a large proportion of acicular ferrite and ensuring the least amount martensite would result in good toughness. Keehan *et al.* (2006a) found that coalesced bainite can be formed in weld metals, which should be detrimental to impact toughness. This will be treated in this thesis.

2. Neural network

The mechanical properties and microstructure can be influenced by a wide variety of parameters, which have their own individual and combined effects. Neural network models are extremely useful in such circumstances, not only

in the study of mechanical properties but wherever the complexity of the problem is overwhelming from a fundamental perspective and where simplification is unacceptable (Bhadeshia, 1999a). The principle of the neural network work utilized here is deeply embedded with Bayesian framework (Mackay 1992a, 1992b, 1994, 1995b) and it is out of scope of this thesis to present it in detail. However, the fundamental structure and important concepts of the neural network are presented below.

2.1 Structure of neural network

A neural network is a powerful nonlinear regression method. It can reveal correlations between large numbers of variables in complex system. It has a transparent structure.

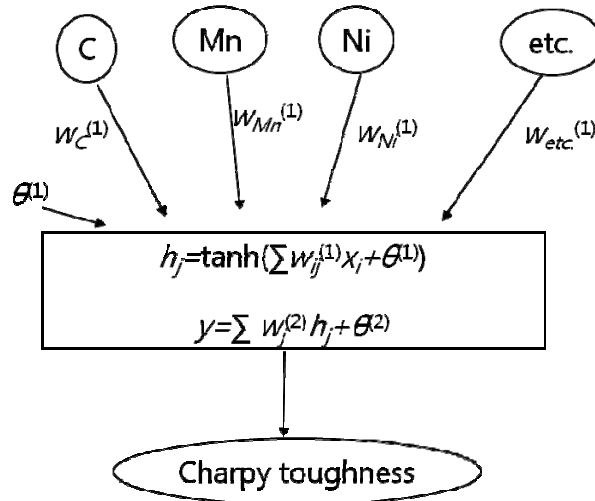


Fig. 1.3: Schematic illustration of the structure of a neural network

In Fig. 1.3, each input x_i is multiplied by a random weight $w_{ij}^{(1)}$ and the products are summed together with a constant $\theta^{(1)}$. The summed products are activated by a tangent hyperbolic function which is chosen because of its flexibility. Then the activated term h_j hidden unit is multiplied by another

weight $w_j^{(2)}$ and summed with a constant $\theta^{(2)}$ to give the output y . In a training process, inputs are given as training data and the maximum number of h_j can be selected. Thus creating a model means finding a proper weight vector \boldsymbol{w} over weight space. Bold font represents vectors (Bhadeshia, 1999a).

2.2 Error estimates

The overall error can be estimated by comparing the predicted values (y_j) of the output against those measured (t_j):

$$E_D \propto \sum_j (t_j - y_j)^2 \quad (1.1)$$

E_D is expected to increase when important variables are missing in the dataset. E_D gives an overall perceived level of noise in the output (Bhadeshia, 1999a). There is a difference between noise and modeling uncertainty (Bhadeshia *et al.*, 2007). Noise results in a different output for the same set of inputs when the experiment is repeated. This is because there are variables which are not controlled so their influence is not included in the analysis. It is measured constant value, thus it cannot help much in assessing the behaviour of the model when extrapolating.

However modeling uncertainty comes from the fact that there may exist many mathematical functions which adequately explain the same set of empirical data but which behave differently in extrapolation. This is well illustrated in Fig. 1.4. At B region where enough data can be used for modelling, different models behaves similarly each other. However, at A region where data is sparse and noisy, thus the modeling uncertainty is clearly large with a lot of variance in the predictions of different functions. Unlike the noise, the magnitude of the modeling uncertainty depends on the position in the input space where a calculation is done. The modeling uncertainty is especially important because it can indicate the region of input space where

further study or experiment is required.

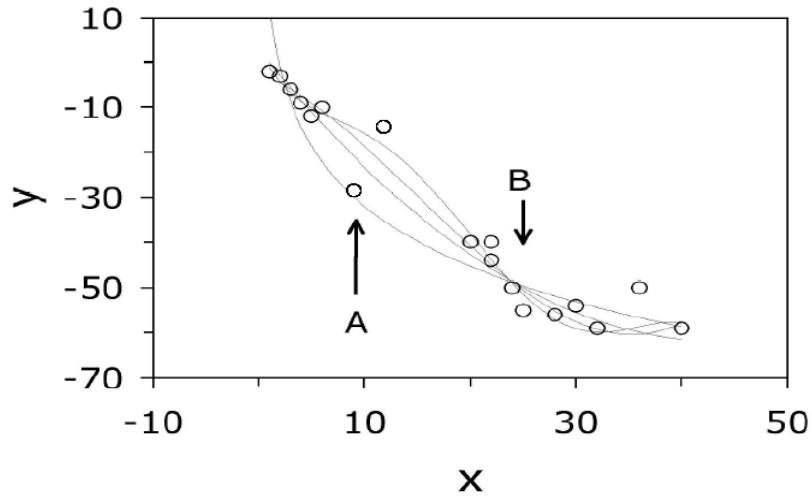


Fig. 1.4: An illustration of how a number of different functions might adequately represent the same set of given data (Bhadeshia *et al.* 2007).

2.3 Overfitting

The problem with neural networks is that a flexible network can be made to fit data even when the latter are noisy. To avoid this, the experimental data can be divided into two groups, a training dataset and test dataset. The model is first produced by using only the training dataset, then its generalization is checked against test data which had not been used in creating the model. Fig. 1.5 shows the evolution of training and test error as a function of the control parameters which determine the complexity of the model.

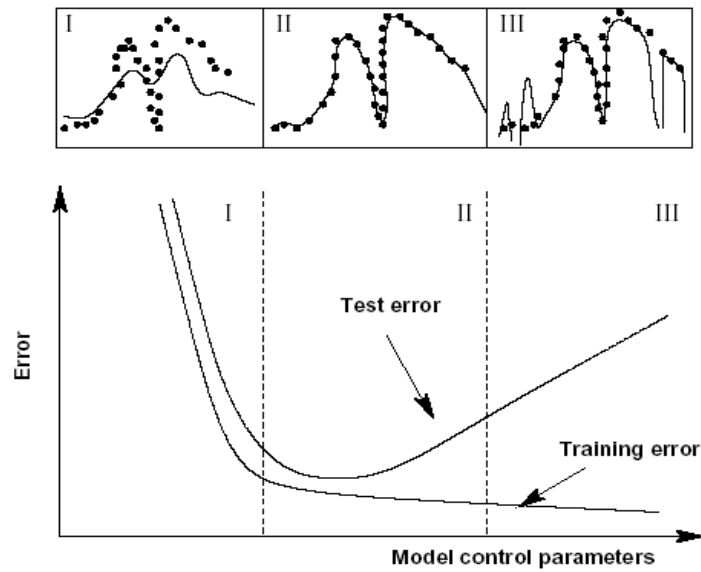


Fig. 1.5: Schematic diagram explaining the optimization of model complexity (MacKay, 1995a)

Even though a model with high complexity is associated with a small training error, it may generalise badly if the model was overfitted. In Fig. 1.5, a proper model should be in the region designated II. In practice, the number of hidden units can be one of the model control parameters (Bhadeshia, 1999a).

2.4 Significance

Neural network based on a bayesian framework can estimate the significance of individual input parameters influencing the outputs (MacKay, 1994). A high value of significance implies that the input parameter concerned explains a relatively large amount of the variation in output and it is not an indication of the sensitivity (Fujii *et al.*, 1996).

2.5 Committee model

The variety of models produced can be ranked according to the magnitude of the test error. The best individual model would then have the minimum test error. However, it is possible in principle to reduce the test error further using the average of predictions from a number of models, *i.e.* a committee of models. Fig. 1.6 illustrates that the test error can be minimized by a committee model which in this case consists of 19 sub-models.

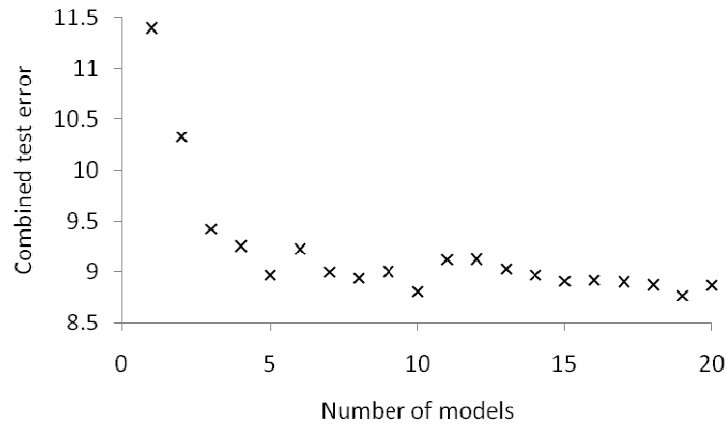


Fig. 1.6: Evolution in the test error with the number of ranked models in the committee (extracted from this work).

The mean prediction \bar{y} of the committee model can be obtained as follows:

$$\bar{y} = \frac{1}{N} \sum_{i=1}^N y_i \quad (1.2)$$

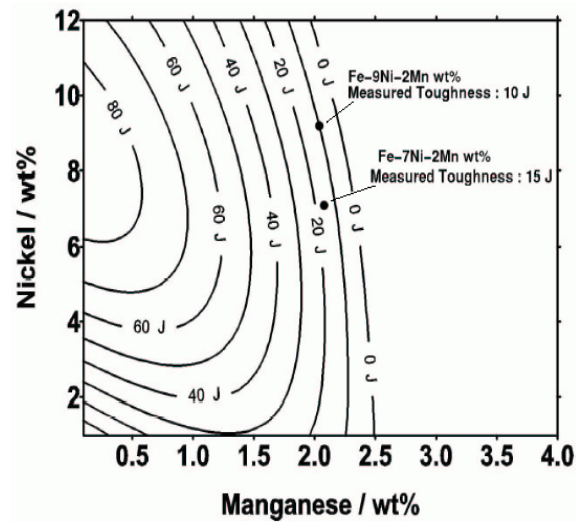
and the associated error in \bar{y} is given by

$$\sigma^2 = \frac{1}{N} \sum_{i=1}^N \sigma_i^2 + \frac{1}{N} \sum_{i=1}^N (y_i - \bar{y})^2 \quad (1.3)$$

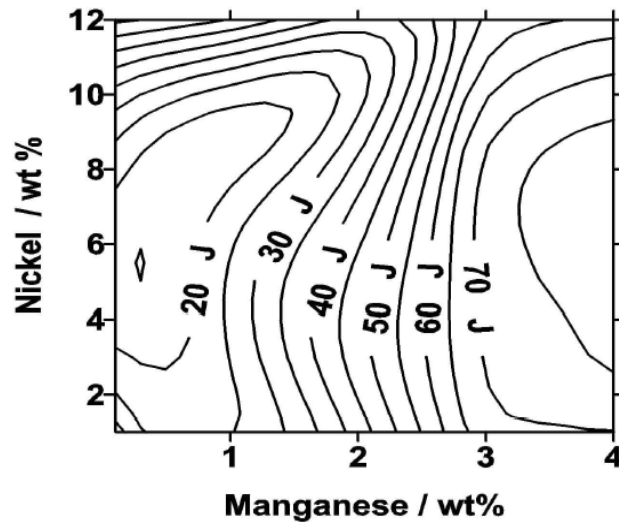
where y_i and σ_i are the prediction value and error of an individual model (MacKay, 1995a).

2.6 An example of application

It has been recognized that adding nickel influences the stacking fault energy of ferrite in such manner that plastic deformation can be accommodated at low temperatures (Svensson, 1994). However in the calculations using a neural network, Muruganath (2002) showed that adding nickel does not in fact improve the toughness at high concentrations of manganese. It was predicted that adding nickel enhances toughness only when the manganese concentration is low (Fig. 1.7). This remarkable result led to further research about the microstructure in low toughness weld metals. Keehan *et al.* (2006a) were able to explain these observations in terms of a coarse constituent found in Fe-7Ni-2Mn wt% weld metal which reduces impact toughness.



(a)



(b)

Fig. 1.7: Effect of manganese and nickel on toughness, as predicted using the neural network models (a) predictions (b) $\pm 1\sigma$ uncertainty in prediction (Muruganath, 2002).

3. Coalesced bainite

3.1 Mechanism

Coalesced bainite has recently become prominent although the original observations were reported in 1979 (Bhadeshia *et al.*, 2006). Its formation mechanism is only qualitatively understood and is summarized in Fig. 1.8.

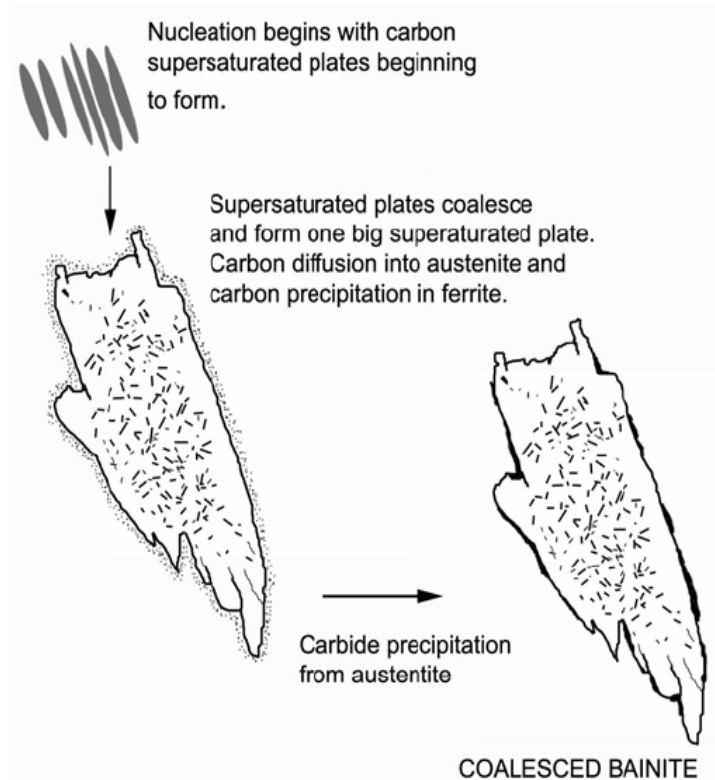


Fig. 1.8: Schematic diagram of the formation of coalesced bainite (Keehan, 2005)

The transformation begins with the formation of the normal small subunits of bainite, but they then coalesce to form a single large plate, followed by the partitioning or precipitation of carbon. The coalescence is accompanied by a thinning of the austenite films between bainite subunits. The films eventually disappear as the subunits develop into the coarser structure. Given that the adjacent subunits all have identical orientation, it is reasonable that they

should combine and grow as a single unit (Chang and Bhadeshia, 1996).

There are two kinds of assumption for coalesced bainite.

- 1) There should be sufficient chemical driving force to bear the larger amount of strain energy associated with a thicker plate.

This condition is satisfied because the transformation occurs at the largest feasible undercooling below B_S . An analysis using a theory for elastically accommodated plates has shown reasonable consistency between the driving force and expected strain energy (Chang and Bhadeshia, 1996).

- 2) There is nothing to stifle the lengthening of the subunits.

This implies that coalescence is only possible at the early stages in the transformation of austenite because the carbon concentration of the austenite increases as transformation progresses then it leads to decreasing in chemical driving force $|\Delta G^{\gamma\alpha}|$. This should render coalescence much less likely (Chang and Bhadeshia, 1996).

There are several reasons why coalesced bainite should form only at low transformation temperatures. The partitioning of carbon from the supersaturated ferrite to austenite is relatively suppressed at low temperatures, permitting the plates to form without any intervening austenite (Bhadeshia *et al.*, 2006). Another reason is that the shape deformation accompanying the growth of bainite is not completely elastically accommodated. The yield strength of all phases is higher at lower temperatures thus the subunits can lengthen longer. This provides a greater opportunity for coalescence to occur (Chang and Bhadeshia, 1996).

3.2 Coalesced bainite in weld metals

Experiments have now confirmed that the coarse, coalesced bainite appears in weld metals alloyed such that the bainite forms at temperature close to the martensite-start temperature (Keehan *et al.*, 2006a). Keehan *et al.* (2006b) also found that the welds with relatively poor toughness always contained the coarse coalesced bainite, whereas the low-Mn high-Ni welds with much better toughness did not.

II. Experiments

1. Neural network modelling

1.1 Collecting data

A extensive database consisting of 5973 combinations of Charpy toughness and 23 inputs including the chemical composition, welding parameters and test temperature was compiled. Welding processes include manual metal arc welding (MMAW), submerged arc welding (SAW), gas tungsten arc welding (GTAW) and gas metal arc welding (GMAW). All data are real experimental results and collected from laboratory experiments and published papers. The sources are listed separately in a reference chapter. About 4000 data were gathered by previous researchers (Muruganath. 2002).

During the collection of data, the concentrations of some elements, for example, chromium, vanadium, copper, cobalt, tungsten, titanium, boron and niobium sometimes were not reported in the published literature. They were treated as zero since the failure to report was taken to mean that there were no deliberate additions.

The heat input was calculated from:

$$\text{heat input} = \frac{VI}{S} \quad (2.1)$$

where V is an arc voltage, I is a current and S is a welding speed.

When the range of acceptable interpass temperature was stated instead of a specific temperature, its averaged value was used. When an interpass temperature was not stated, it was assumed to be 200 °C if the joint geometry corresponded to ISO 2560.

For the post-weld heat treatment, the opinion of Dr. Leif Karlsson in ESAB AB (Sweden) was respected. He explained that heat treatments below 500 °C

are not post-weld heat treatments (PWHT) intended to modify structure and properties and for steels PWHT is rarely done below 500 °C. Thus PWHT below 500 °C were considered to correspond to the as-welded condition, where PWHT temperature and time were set as 20 °C and 0 h, respectively.

D_{Fe} is a calculated variable included as a representation of iron diffusion during post-weld heat treatment:

$$D_{Fe} = 3600 \times \text{pwht} \times \exp\left(\frac{-Q}{RT}\right) \quad (2.2)$$

where Q , R and T correspond to a activation energy for the self-diffusion of iron, gas constant and absolute temperature, respectively:

$$Q = 260000 \text{ J mol}^{-1}$$

$$R = 8.31 \text{ J K}^{-1} \text{ mol}^{-1}$$

$$T = 273.15 + \text{pwhtT}(\text{°C})$$

However, when original D_{Fe} values were used as input parameters, the computations did not recognize them properly because the numbers ranged over many orders of magnitude. Thus the values of D_{Fe} multiplied by 10^{22} were used, normalized between -0.5 and 0.5 as follows:

$$x_n = \frac{x - x_{min}}{x_{max} - x_{min}} - 0.5 \quad (2.3)$$

where x_n is the normalized value, x is the real value, and x_{min} and x_{max} are minimum and maximum values of the data set, respectively.

1.2 The analysis of database

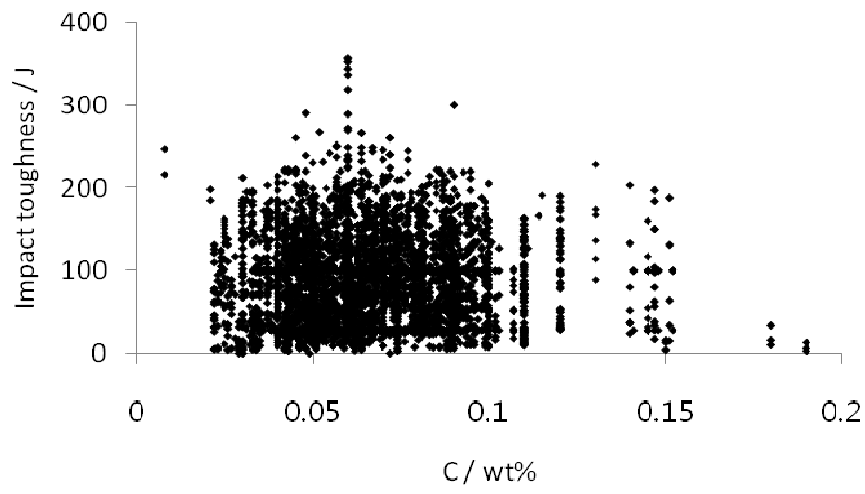
The information of database is listed in Table 2.1

Table 2.1 The information of database

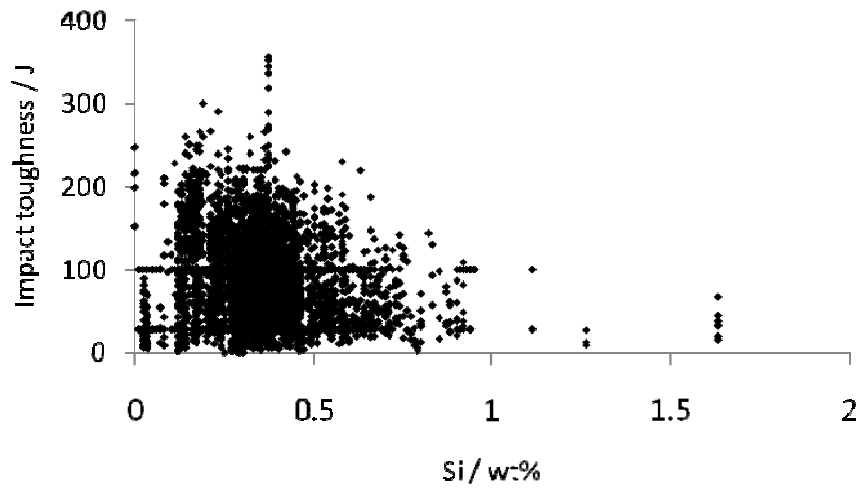
Variable	Range	Mean	Standard deviation
C/wt%	0.008-0.19	0.07	0.02
Si/wt%	0-1.63	0.35	0.14
Mn/wt%	0-2.31	1.20	0.40
S/wt%	0.002-0.14	0.01	0.01
P/wt%	0-0.25	0.01	0.01
Ni/wt%	0-12.40	0.88	1.83
Cr/wt%	0-19.50	0.35	1.19
Mo/wt%	0-2.43	0.20	0.31
V/wt%	0-0.53	0.01	0.03
Cu/wt%	0-2.18	0.08	0.21
Co/wt%	0-0.092	0.003	0.01
W/wt%	0-3.86	0.004	0.11
O/ppmw	25-1700	429	161
Ti/ppmw	0-770	71	115
N/ppmw	0-1000	95	67
B/ppmw	0-200	8	27
Nb/ppmw	0-1770	32	109
HI/kJmm ⁻¹	0.21-16.36	1.49	0.83
IT/ °C	20-350	182	39
PWHTT/ °C	20-940	198	287
PWHTt/h	0-100	1.3	4.2
D _{Fe}	0-3.68 × 10 ¹²	6.22 × 10 ¹⁰	4.47 × 10 ¹¹
TT/ °C	-196-136	-34.5342	36
Charpy toughness/J	0.1-356	85	50

ppmw: Part per million by weight
 HI: Heat input IT: Interpass temperature
 PWHTT: Post-weld heat treatment temperature
 PWHTt: Post-weld heat treatment time
 D_{Fe}: A variable for iron diffusion during post-weld heat treatment
 TT: Test temperature

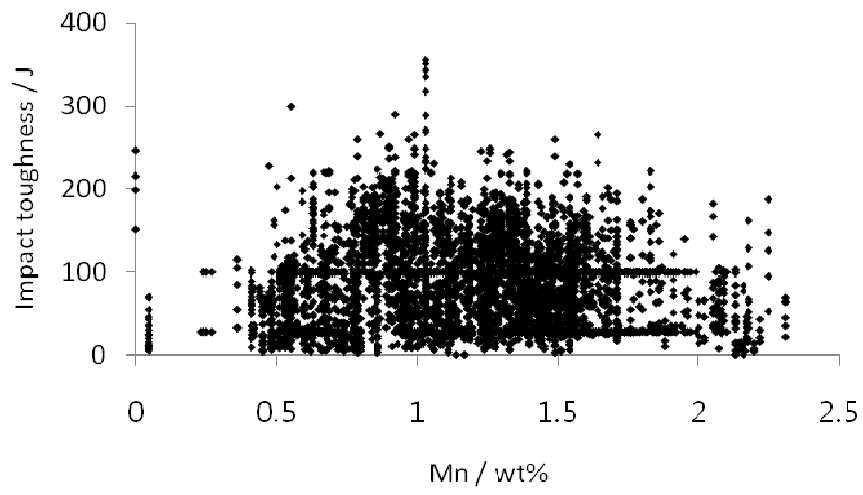
Fig.2.1 shows the distribution of used data. Carbon, manganese, nickel, oxygen and interpass temperature *etc.* were expected to have balanced uncertainties since they were well distributed relatively.



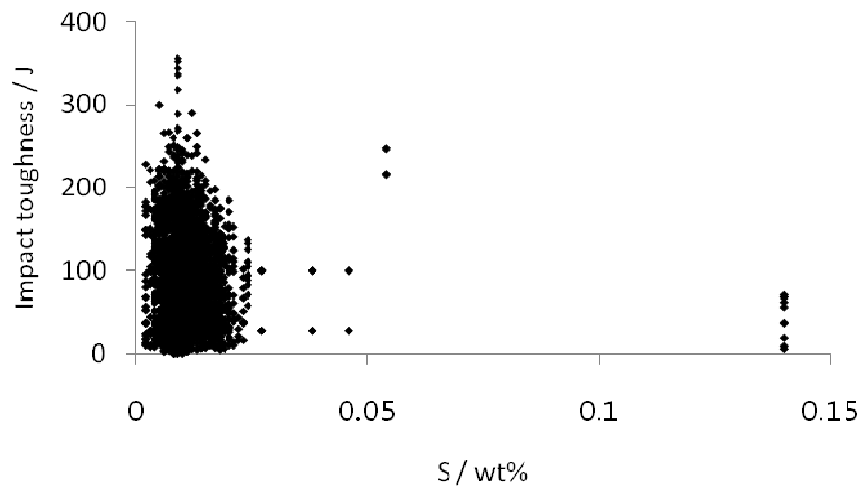
(a)



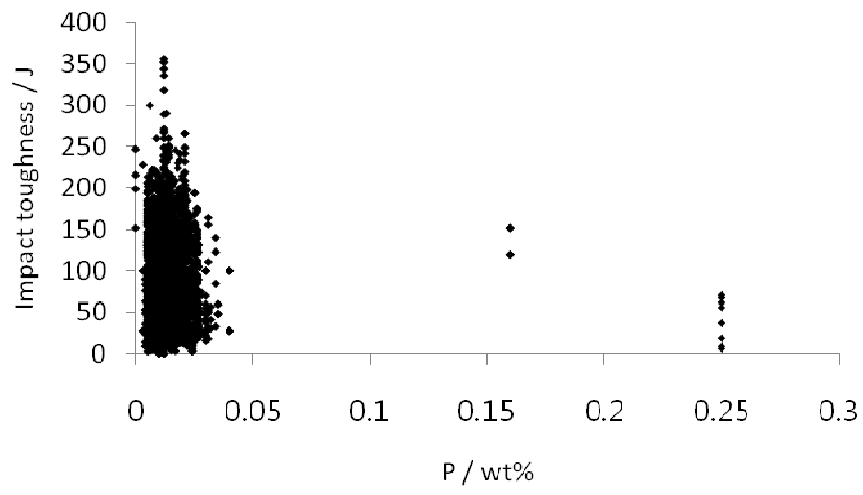
(b)



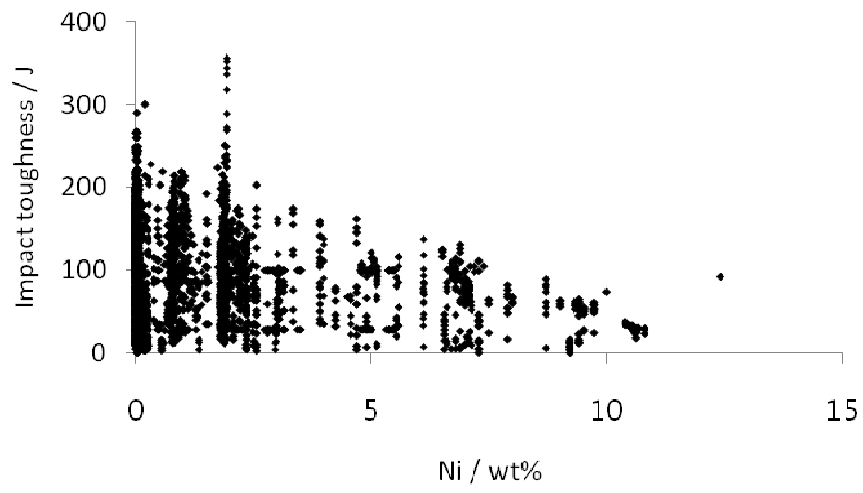
(c)



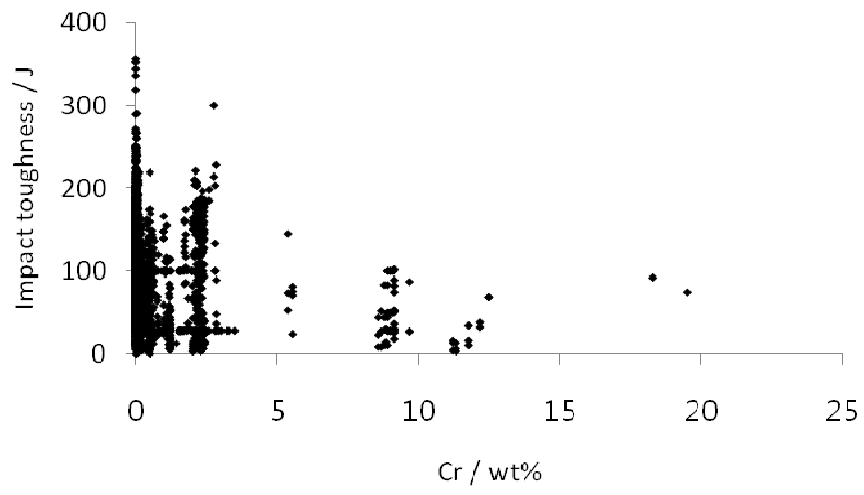
(d)



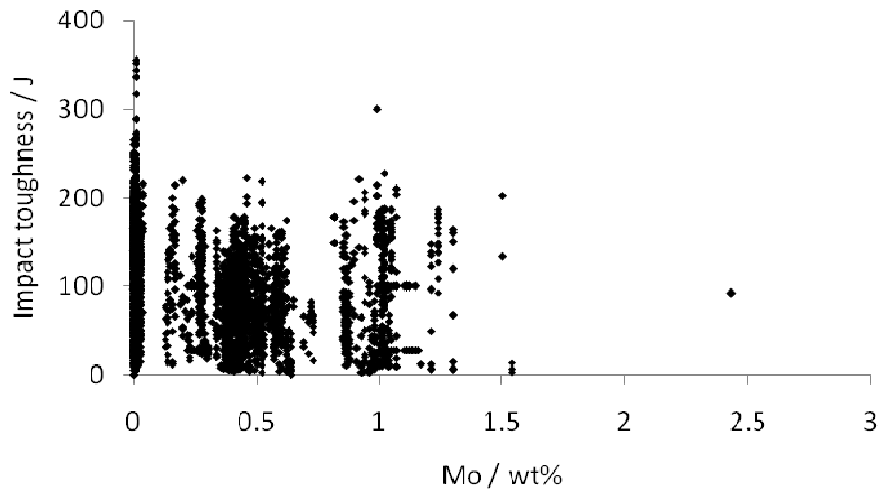
(e)



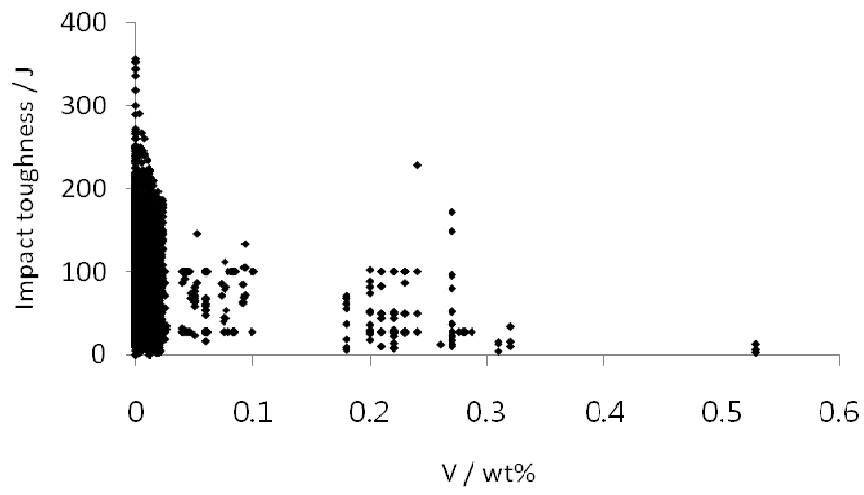
(f)



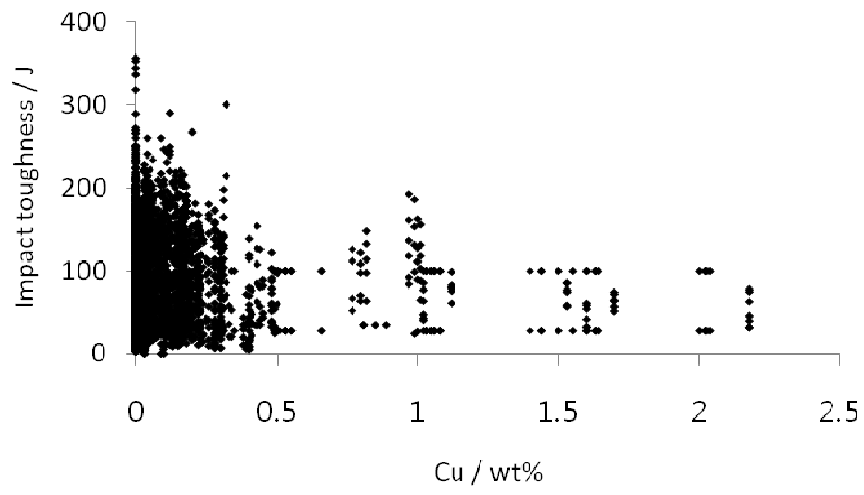
(g)



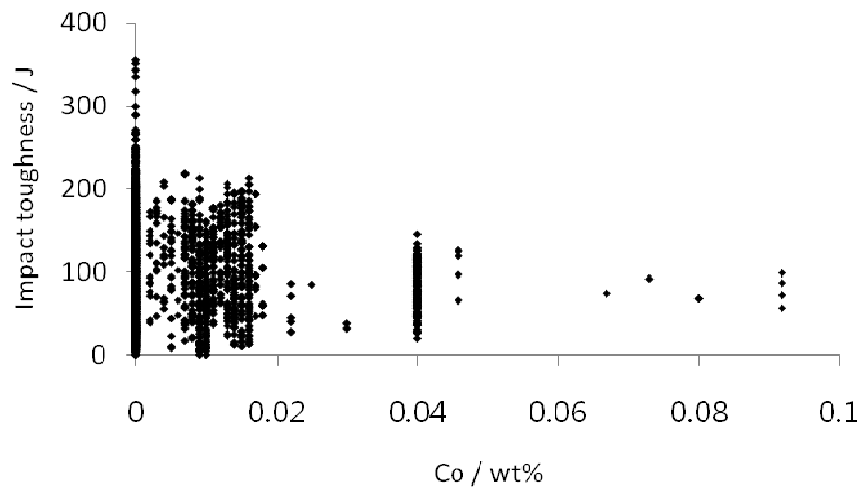
(h)



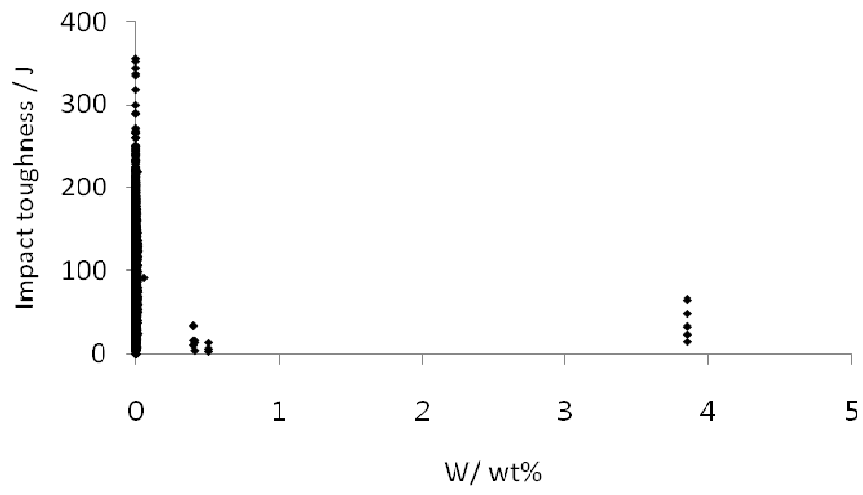
(i)



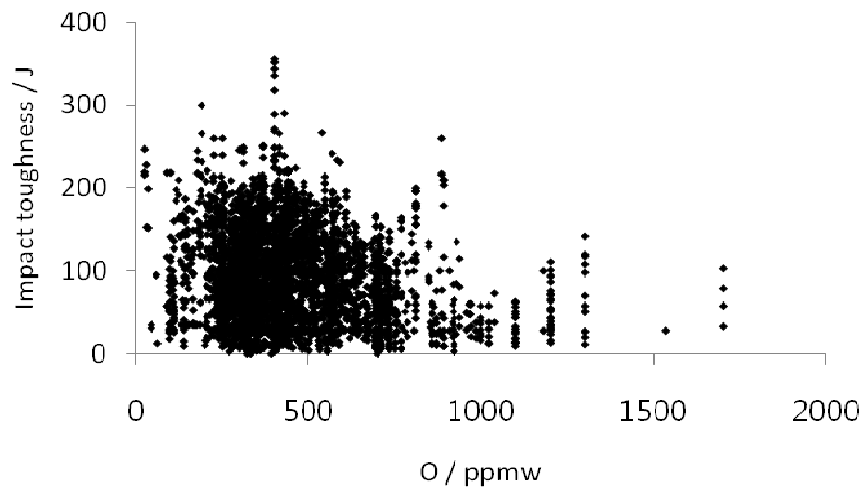
(j)



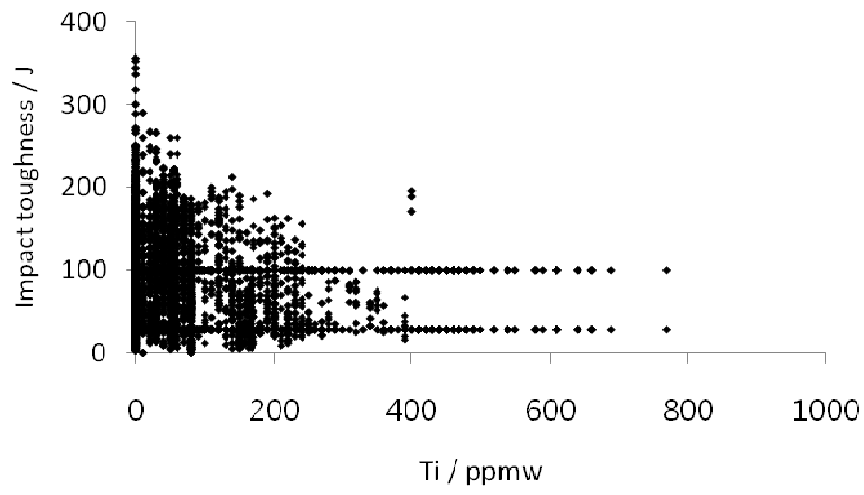
(k)



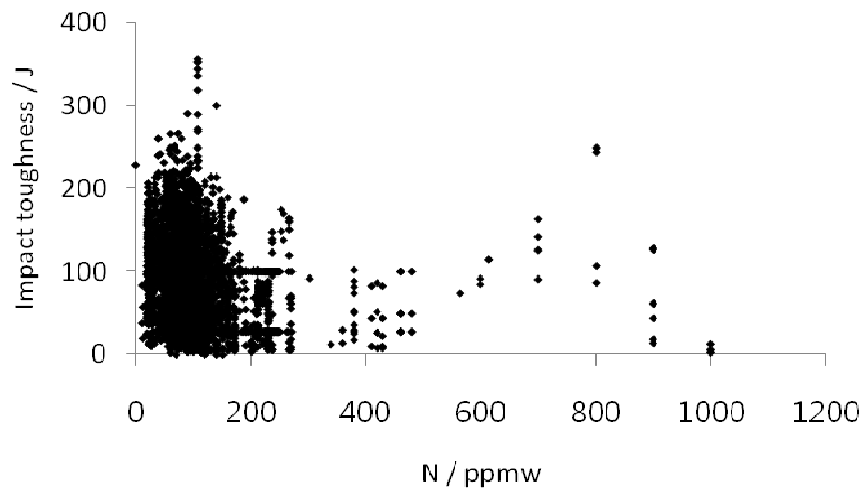
(l)



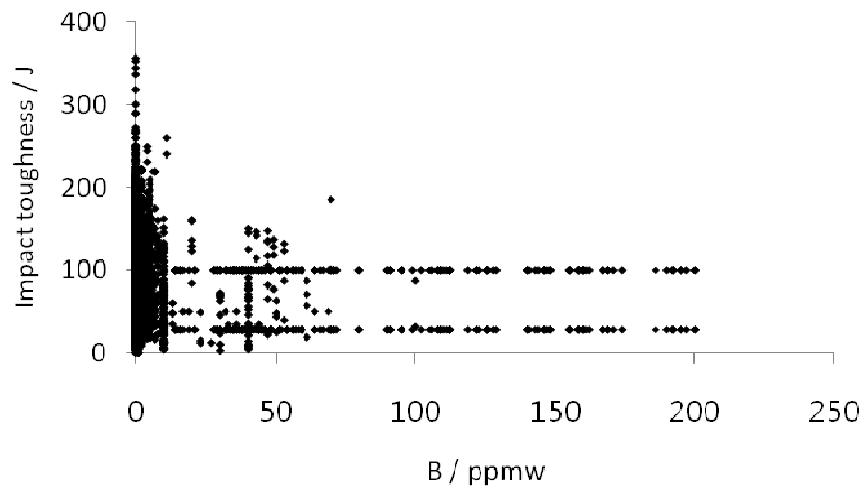
(m)



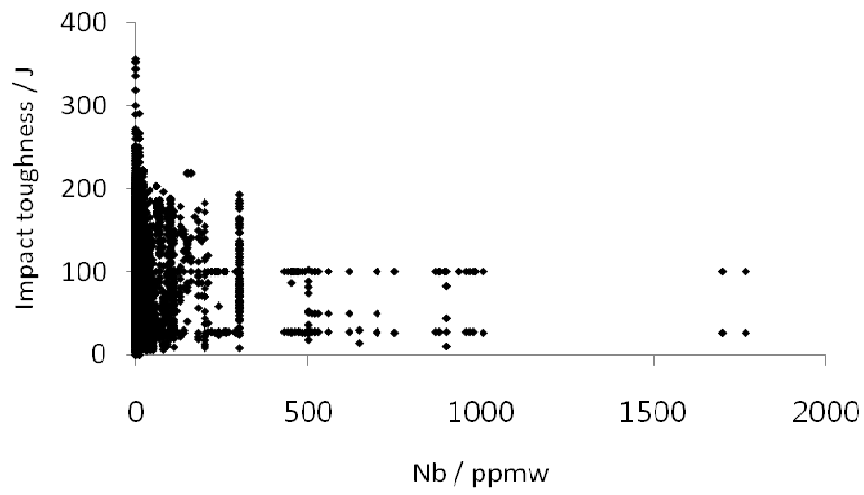
(n)



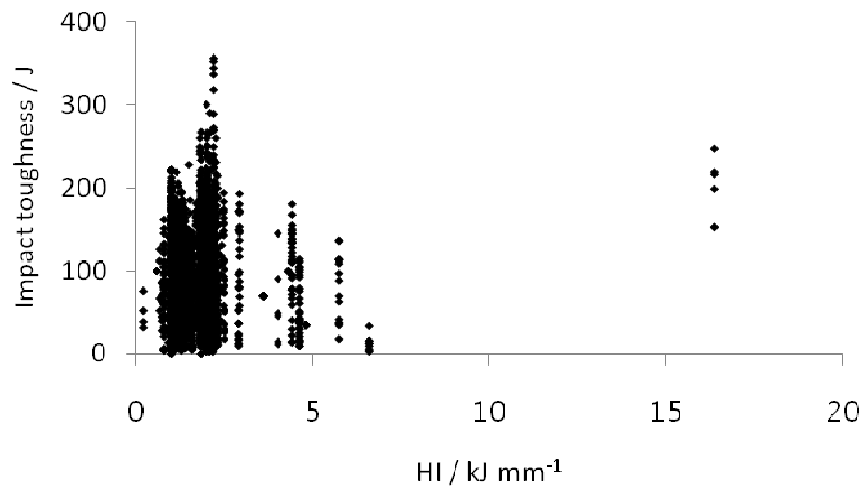
(o)



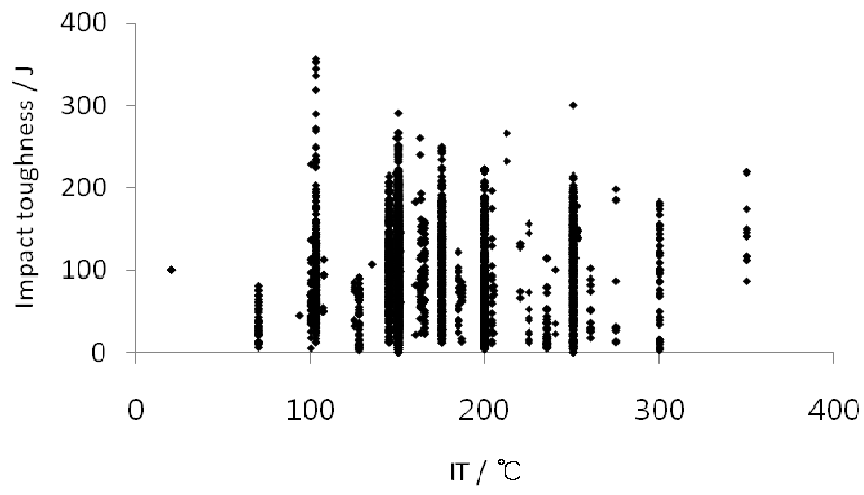
(p)



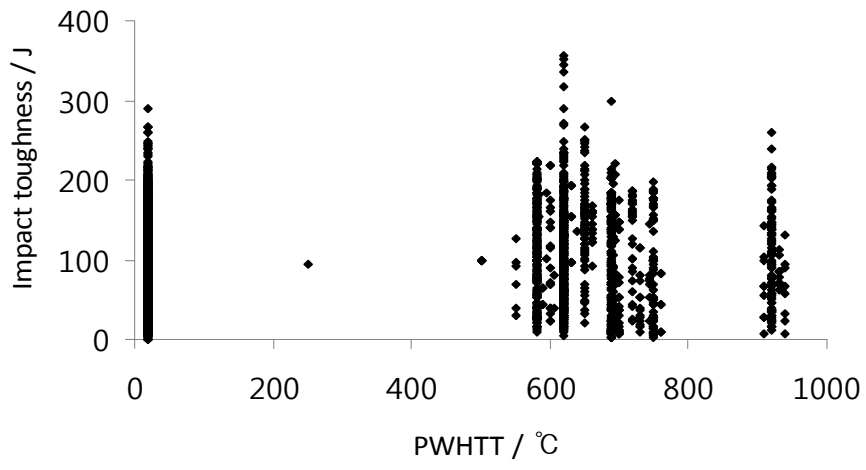
(q)



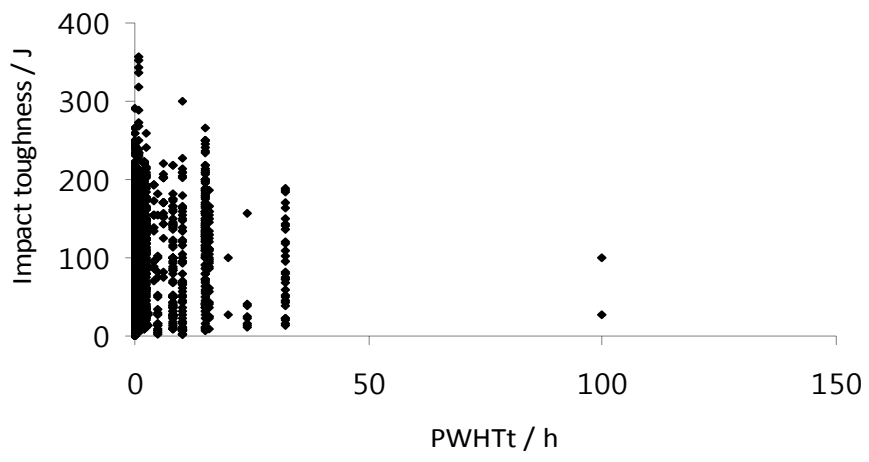
(r)



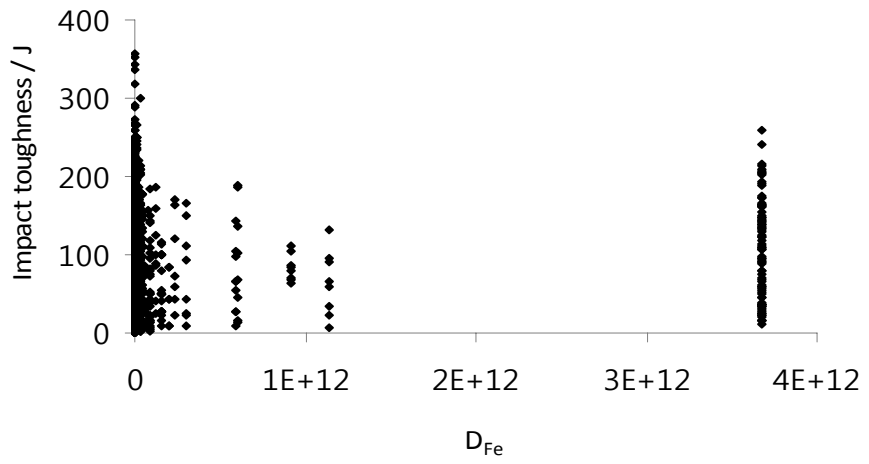
(s)



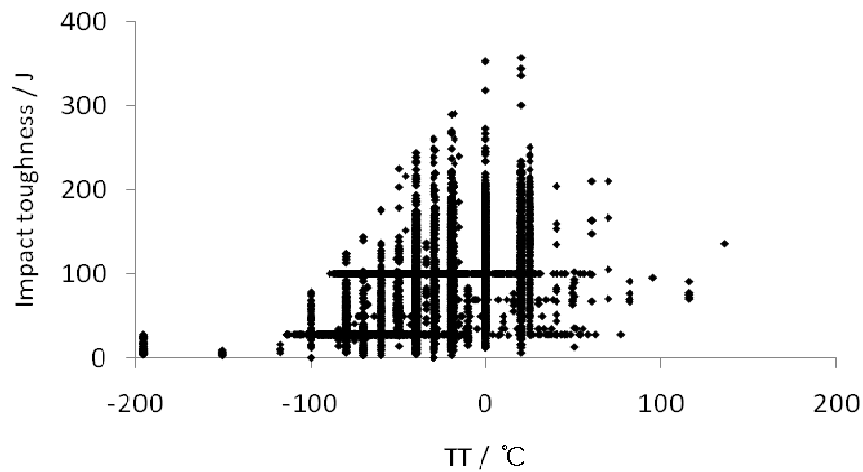
(t)



(u)



(v)



(w)

Fig. 2.1: Distribution of individual input parameters in database.

2. Coalesced bainite

2.1 Weld metal

Based on Keehan's work (2006a), two kinds of weld metal were prepared by ESAB AB (Sweden), 2Mn, 0.5Mn respectively (Table 2.2).

Table 2.2 Compositions of weld metal (wt%)

	C	Si	Mn	P	S	Cr	Ni	Mo	W
2Mn	0.03	0.23	2.05	0.01	0.008	0.43	7.1	0.63	0.004
0.5Mn	0.025	0.39	0.58	0.01	0.009	0.15	6.5	0.39	0.001
	Co	V	Nb	Cu	Al	Ti	B	O	N
2Mn	0.008	0.021	0.004	0.02	0.001	0.011	0.0012	0.031	0.011
0.5Mn	0.009	0.018	0.002	0.02	0.001	0.015	0.0012	0.033	0.009

2.2 Dilatometer

Cylindrical dilatometric samples of diameter 3 mm and length 10 mm were machined from both weld metals with their longitudinal directions parallel to

that of welding. A push-rod BAHR DIL805 high-speed dilatometer with radio frequency induction heating was used. The sample temperature is recorded by a thermocouple welded to its surface. For determining the martensite-start temperature (M_s), a temperature profile was designed to heat up the sample to 1100 °C for 3 minutes followed by cooling using helium gas at a variety of rates: -150, -125, -100, -75 and -50 °C s⁻¹. For isothermal transformation, following austenisation at 1100 °C for 5 minutes and each sample was cooled down to the target temperature within 7 s. Each sample was used only once.

2.3 Hardness tests

Hardness can be used as supporting evidence in the determination of M_s . The stated value corresponds to an average of ten measurements made at random location on each sample.

2.4 Microscopy

Metallography was conducted on the samples used in the dilatometer experiments. They were mounted in Bakelite, wet ground, polished to 0.25 µm diamond paste and etched using 2% nital etchant for light optical microscopy and field-emission gun scanning electron microscopy.

III. Determination of the martensite-start temperature

An accurate determination of the martensite-start temperature (M_S) is important because coalesced bainite is known to form in circumstances where the bainite-start temperature (B_S) is close to M_S (Keehan *et al.* 2006). Chang and Bhadeshia (1996) reported that coalescence occurred in a sample transformed isothermally at a temperature which is just 10K above M_S . The offset method developed by Yang and Bhadeshia (2007) was used to interpret dilatometric data because it provides an objective method for extracting reproducible information regarding the transformation-start temperature.

1. The transformation-start temperature

Since the martensite transformation is generally an athermal transformation, it should be independent of the cooling rate, especially in ordinary low-alloy steels and within the cooling capabilities of the dilatometer used. Consequently, it should be possible to determine M_S from the point at which the transformation-start temperature ($T_S^{\gamma\alpha}$) ceases to change as the cooling rate is increased.

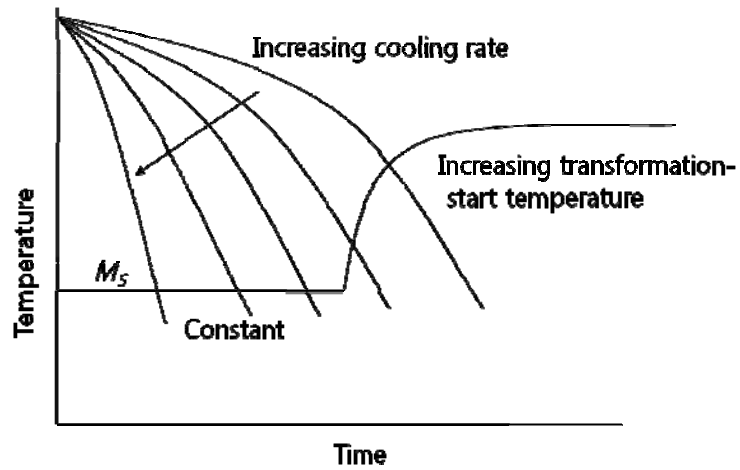
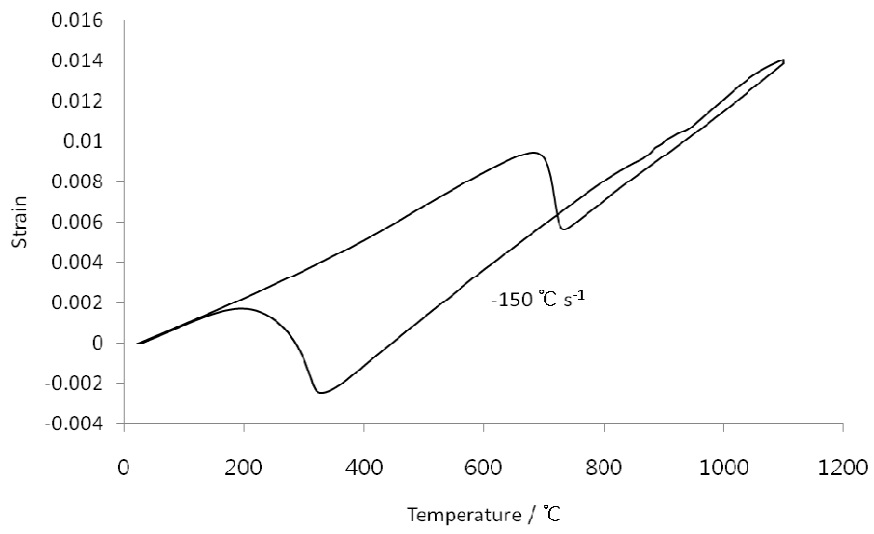


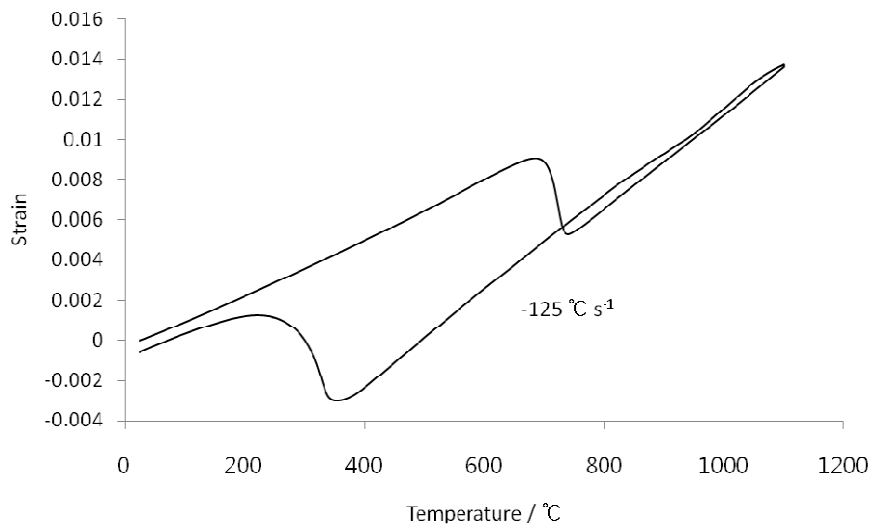
Fig. 3.1: Schematic diagram showing that M_S corresponds the point at which T_S^{90} ceases to change as the cooling rate is increased.

1.1 The 2Mn alloy

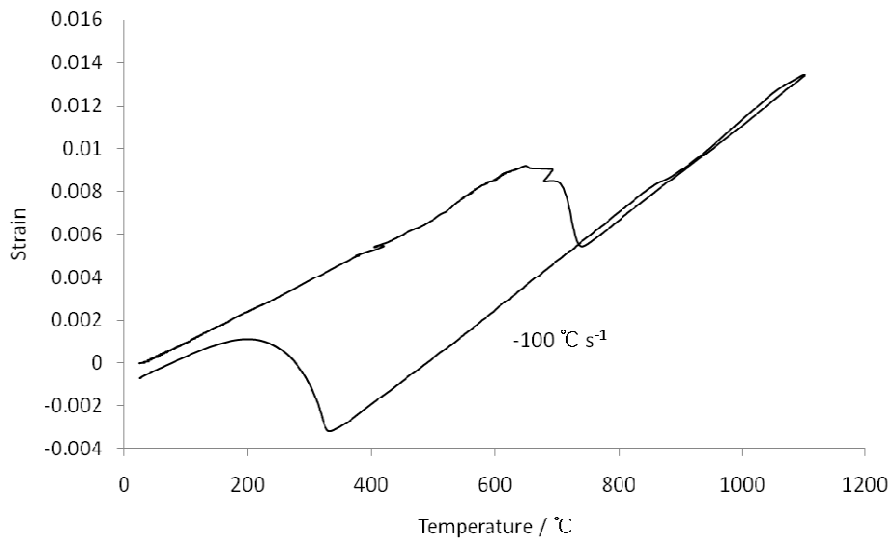
Fig. 3.2 shows the dilatometric curves of the 2Mn alloy for each cooling rate. Strain is the ratio of dilatation length to the original length (10 mm) of sample.



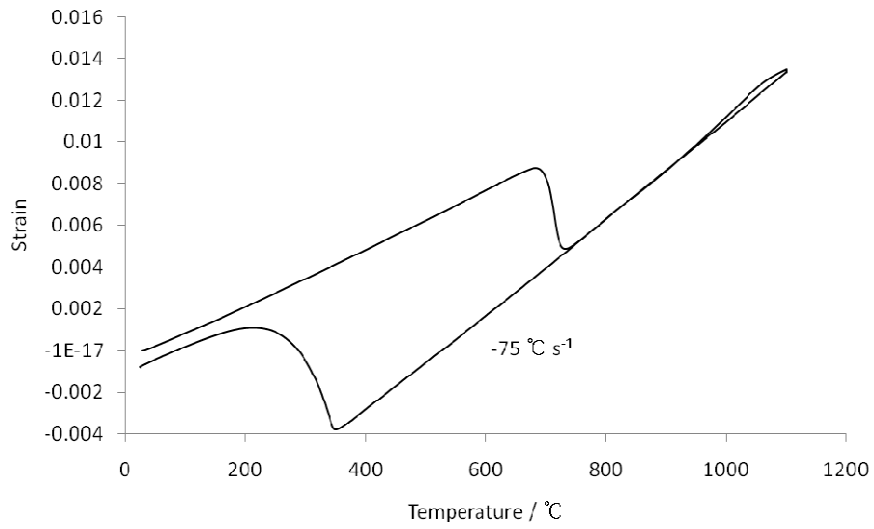
(a) $-150\text{ }^{\circ}\text{C s}^{-1}$



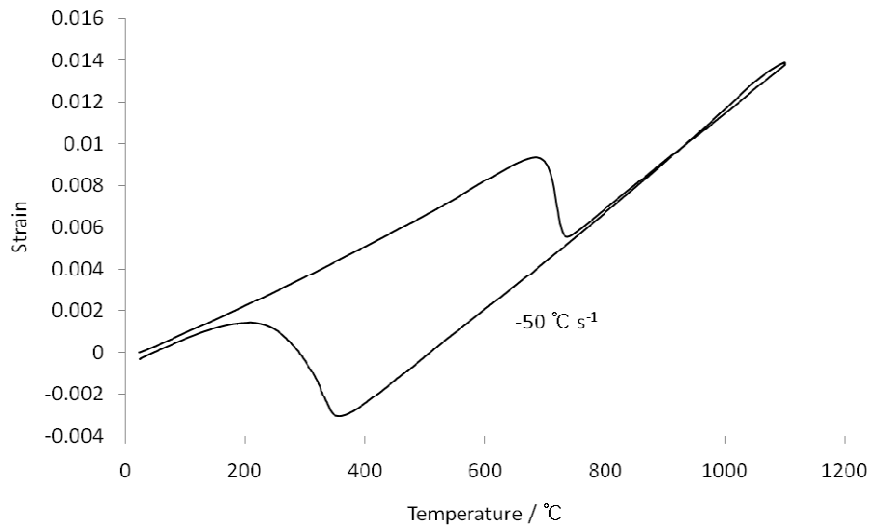
(b) $-125\text{ }^{\circ}\text{C s}^{-1}$



(c) $-100\text{ }^{\circ}\text{C s}^{-1}$



(d) $-75\text{ }^{\circ}\text{C s}^{-1}$



(e) $-50 \text{ }^{\circ}\text{C s}^{-1}$

Fig. 3.2: Dilatation curves of the 2Mn alloy for each cooling rate (a) $-150 \text{ }^{\circ}\text{C s}^{-1}$ (b) $-125 \text{ }^{\circ}\text{C s}^{-1}$ (c) $-100 \text{ }^{\circ}\text{C s}^{-1}$ (d) $-75 \text{ }^{\circ}\text{C s}^{-1}$ (e) $-50 \text{ }^{\circ}\text{C s}^{-1}$

All curves maintained a linear profile during cooling, which means that the martensitic transformation was not interrupted by any other reaction. The A_{C1} temperature was also measured by the offset method (Yang and Bhadeshia, 2007) to compare with A_{e1} calculated using *MTDATA* based on chemical composition of Table 2.2 in chapter 2. The calculation used *MTDATA for Window version 4.74* and the *TCFE:TCAB database for steels v1.0-6 September 2001*. The phases allowed to exist were FCC_A1, BCC_A2 and CEMENTITE. All elements were forced into equilibrium. The temperature at which CEMENTITE disappears was used as the A_{e1} temperature. In this way, the measured A_{C1} and calculated A_{e1} temperatures were found to be $674 \text{ }^{\circ}\text{C} \pm 5 \text{ }^{\circ}\text{C}$ and $444 \text{ }^{\circ}\text{C}$.

Fig. 3.3 shows the change of $T_S^{\gamma\alpha}$ with the magnitude of the cooling rate.

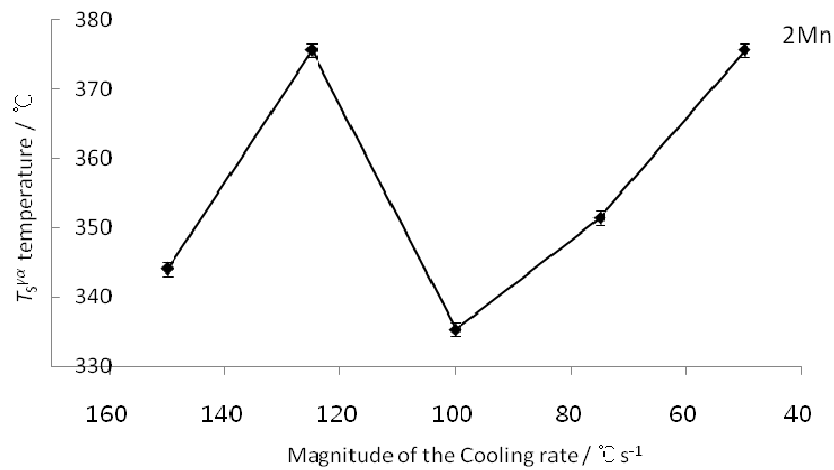


Fig. 3.3: Variation of $T_s^{\gamma\alpha}$ of the 2Mn alloy with the magnitude of the cooling rate.

There are irregular trends as a function of cooling rate, with $T_s^{\gamma\alpha}$ for $-125 \text{ }^\circ\text{C s}^{-1}$ being as high as that for $-50 \text{ }^\circ\text{C s}^{-1}$. However the dilatation curve for $-125 \text{ }^\circ\text{C s}^{-1}$ could not be faulted as shown in Fig. 3.2 (b).

As a precaution, the overall chemical composition of the $-125 \text{ }^\circ\text{C s}^{-1}$ sample was chemically analyzed. The results in Table 3.1 show that the composition of the sample is identified to that of the weld metal. The results illustrated in Fig. 3.3 are therefore considered to be correct in spite of the scatter.

Table 3.1 Composition of weld metal and that of the $-125 \text{ }^\circ\text{C s}^{-1}$ sample (wt%)

	Mn	Ni	Si
2Mn weld metal	2.05	7.1	0.23
$-125 \text{ }^\circ\text{C s}^{-1}$ sample	1.98	7.04	0.392

Measured hardness values of 2Mn in Fig. 3.4 were more interesting. All samples have eventually the same hardness. Furthermore, the slowest cooling

rate produced as hard a microstructure as the other samples within the observed scatter.

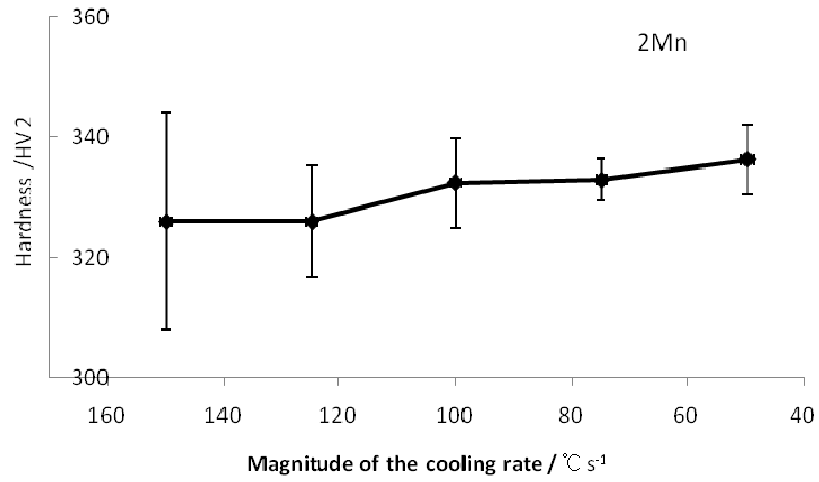
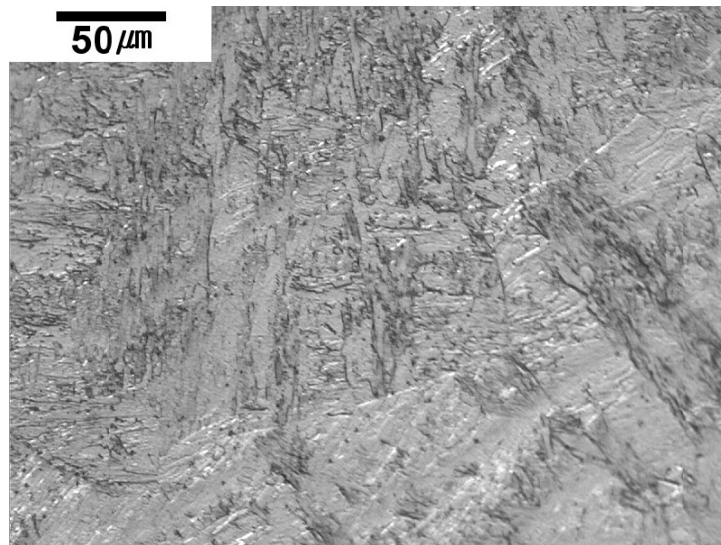
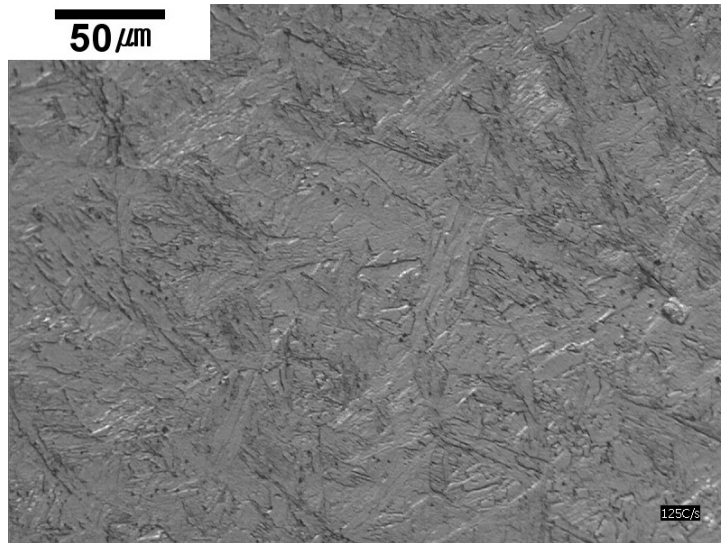


Fig. 3.4: Variation of hardness of the 2Mn alloy with the magnitude of the cooling rate

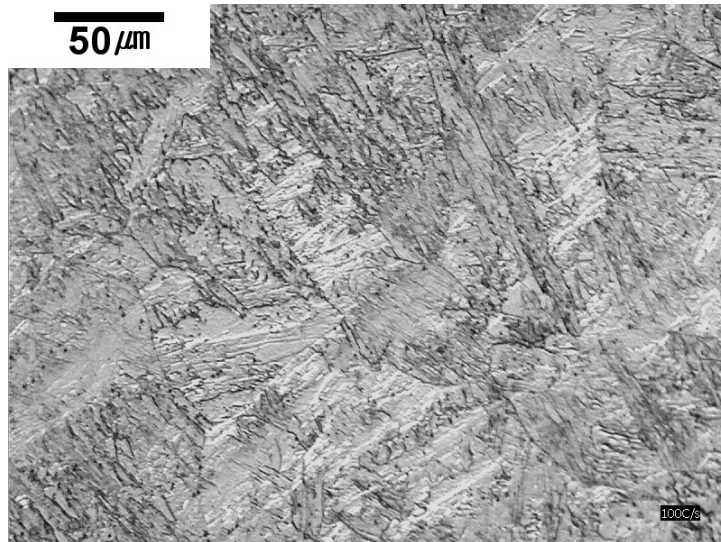
Optical micrographs for each of the samples are shown in Fig. 3.5.



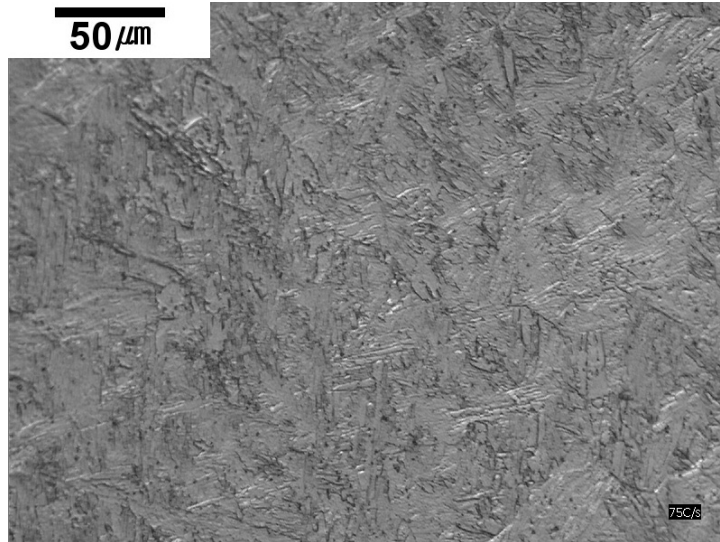
(a) -150 °C s⁻¹



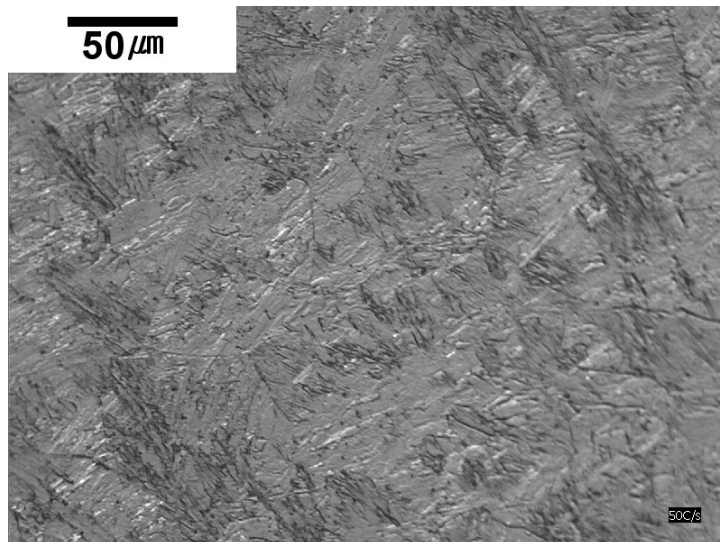
(b) $-125\text{ }^{\circ}\text{C s}^{-1}$



(c) $-100\text{ }^{\circ}\text{C s}^{-1}$



(d) $-75\text{ }^{\circ}\text{C s}^{-1}$



(e) $-50\text{ }^{\circ}\text{C s}^{-1}$

Fig. 3.5: Optical micrographs of dilatometric samples cooled at (a) $-150\text{ }^{\circ}\text{C s}^{-1}$ (b) $-125\text{ }^{\circ}\text{C s}^{-1}$ (c) $-100\text{ }^{\circ}\text{C s}^{-1}$ (d) $-75\text{ }^{\circ}\text{C s}^{-1}$ (e) $-50\text{ }^{\circ}\text{C s}^{-1}$

All the micrographs show similar microstructures consistent with a

martensitic state and it is particularly relevant that there is no obvious difference between -150 and -50 $^{\circ}\text{C s}^{-1}$ samples. It cannot therefore be assumed that the cooling curve of -50 $^{\circ}\text{C s}^{-1}$ fell into the increasing temperature region of Fig. 3.1.

To conclude, the $T_S^{\gamma\alpha}$ temperatures of all cooling rates are consistent with the constant temperature region. Table 3.2 shows the full set of results from the $T_S^{\gamma\alpha}$ analysis for each cooling curve. Different offsets correspond to the results from individual tangent lines those were produced from different temperature regions during cooling, $400-430$ $^{\circ}\text{C}$, $400-460$ $^{\circ}\text{C}$ and $400-500$ $^{\circ}\text{C}$.

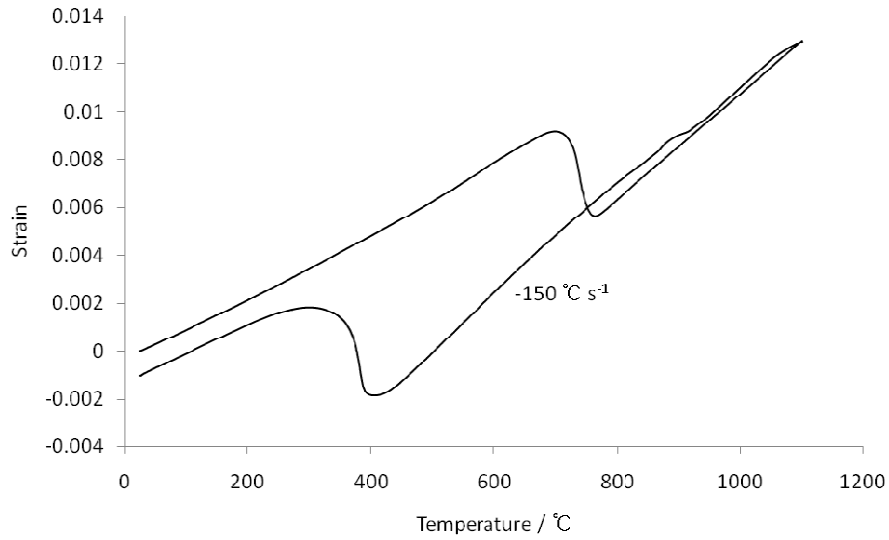
Table 3.2 All $T_S^{\gamma\alpha}$ temperatures of the 2Mn alloy for each cooling curve ($^{\circ}\text{C}$)

	offset1	offset2	offset3	average	standard deviation
150 $^{\circ}\text{C s}^{-1}$	344	344	344	344	0
125 $^{\circ}\text{C s}^{-1}$	375	376	376	376	0.6
100 $^{\circ}\text{C s}^{-1}$	333	336	337	335	2.1
75 $^{\circ}\text{C s}^{-1}$	351	351	352	351	0.2
50 $^{\circ}\text{C s}^{-1}$	375	376	376	376	0.6
Total				356	17

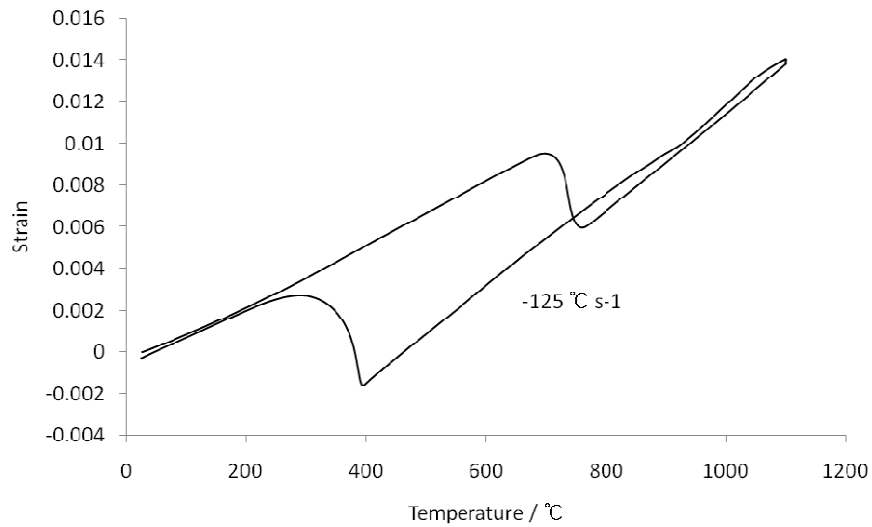
In conclusion, the M_S of the 2Mn alloy can finally be set at 356 $^{\circ}\text{C} \pm 17$ $^{\circ}\text{C}$.

1.2 The 0.5Mn alloy

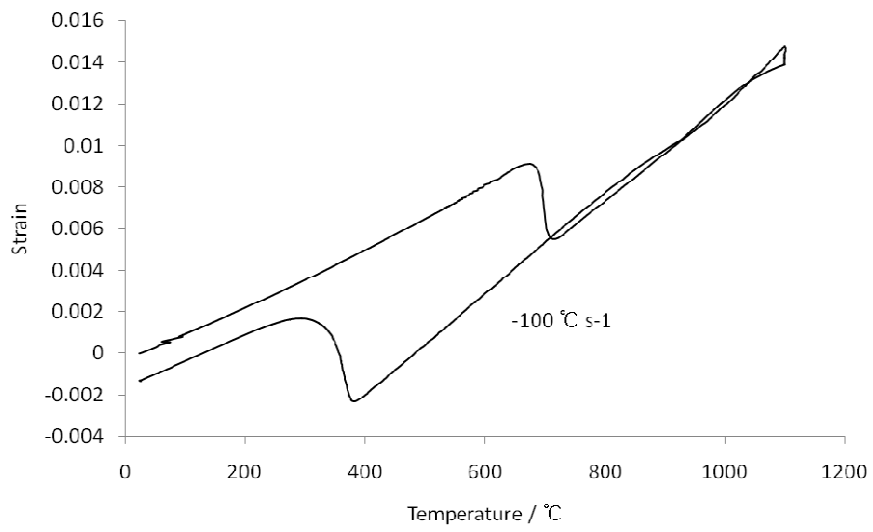
The same analysis was performed on the 0.5Mn alloy. Fig. 3.6 shows the dilatometric curves for each cooling rate.



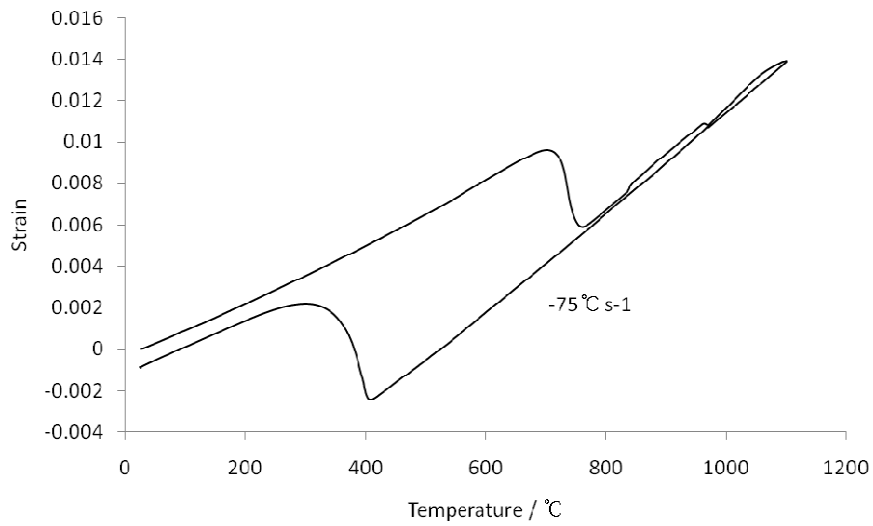
(a) -150 °C s^{-1}



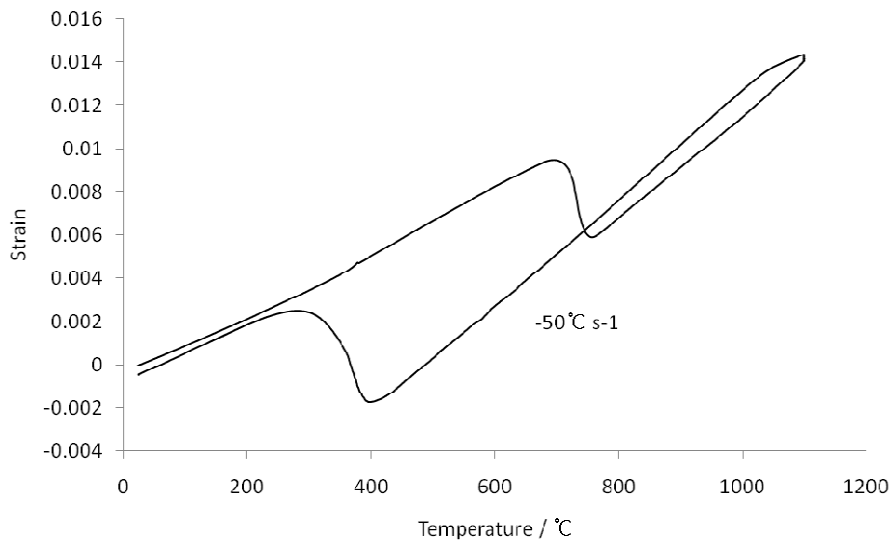
(b) -125 °C s^{-1}



(c) -100 °C s⁻¹



(d) -75 °C s⁻¹



(e) $-50 \text{ } ^\circ\text{C s}^{-1}$

Fig. 3.6: Dilatation curves of the 0.5Mn alloy for each cooling rate (a) $-150 \text{ } ^\circ\text{C s}^{-1}$ (b) $-125 \text{ } ^\circ\text{C s}^{-1}$ (c) $-100 \text{ } ^\circ\text{C s}^{-1}$ (d) $-75 \text{ } ^\circ\text{C s}^{-1}$ (e) $-50 \text{ } ^\circ\text{C s}^{-1}$

All of them are well-behaved in the cooling stages. Following the procedure for the case of the 2Mn alloy, A_{C1} and A_{e1} temperatures were $685 \text{ } ^\circ\text{C} \pm 8.4 \text{ } ^\circ\text{C}$ and $561 \text{ } ^\circ\text{C}$, respectively.

Fig. 3.7 shows the change of $T_S^{\gamma\alpha}$ of the 0.5Mn alloy with the magnitude of the cooling rate.

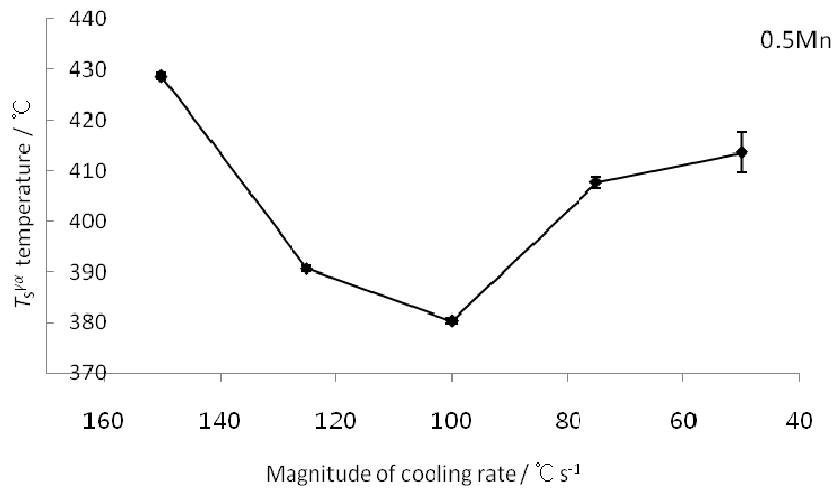


Fig. 3.7: Variation of $T_S^{\gamma\alpha}$ of the 0.5Mn alloy with the magnitude of the cooling rate.

The highest cooling rate produced the highest $T_S^{\gamma\alpha}$, which is contradictory to the theory in Fig. 3.1. However, as confirmed, the dilatation curve of $-150 \text{ }^\circ\text{C s}^{-1}$ cannot be faulted.

In Fig. 3.8 the hardness of $-150 \text{ }^\circ\text{C s}^{-1}$ sample is lower relatively than those of other cooling rates; however, it is within the standard deviation of the measurements. There is no reason therefore to exclude the $T_S^{\gamma\alpha}$ of $-150 \text{ }^\circ\text{C s}^{-1}$ in determining M_S .

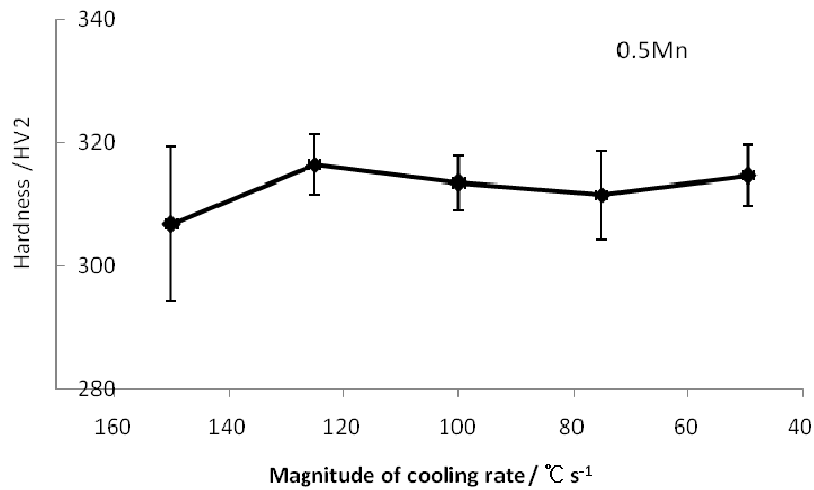


Fig. 3.8: Variation of hardness of the 0.5Mn alloy with the magnitude of the cooling rate

It is noticeable that the lowest cooling rate also produced hard structure with a small deviation. Therefore all the $T_S^{\gamma\alpha}$ temperatures were assumed to be in the constant temperature region in Fig. 3.1 thus used to fix the M_S of 0.5Mn. The results are listed in Table 3.2.

Table 3.3 All $T_S^{\gamma\alpha}$ temperatures of the 0.5Mn alloy for each cooling curve (°C)

	offset1	offset2	offset3	average	standard deviation
150 °C s ⁻¹	428	429	429	429	0.6
125 °C s ⁻¹	390	391	391	391	0.6
100 °C s ⁻¹	380	380	381	380	0.6
75 °C s ⁻¹	407	407	409	408	1.2
50 °C s ⁻¹	409	416	416	414	4.0
Total				404	19

The estimated M_S of the 0.5Mn alloy was determined to be 404 °C ± 19 °C.

2. Discussion about the high $T_S^{\gamma\alpha}$

Further analysis was conducted of the dilatometric data to study the development of transformation below $T_S^{\gamma\alpha}$. In Figs. 3.9 and 3.10, only those data are replotted which are below $T_S^{\gamma\alpha}$. It is seen that transformation rate is suppressed in the 2Mn samples cooled at -150 , -125 and -50 $^{\circ}\text{C s}^{-1}$ and in the 0.5 Mn samples cooled at -150 and -50 $^{\circ}\text{C s}^{-1}$.

It is speculated that remaining samples may contain a level of microscopic chemical segregation which permits transformation to proceed more rapidly once initiated. After all, welds do not solidify under equilibrium condition.

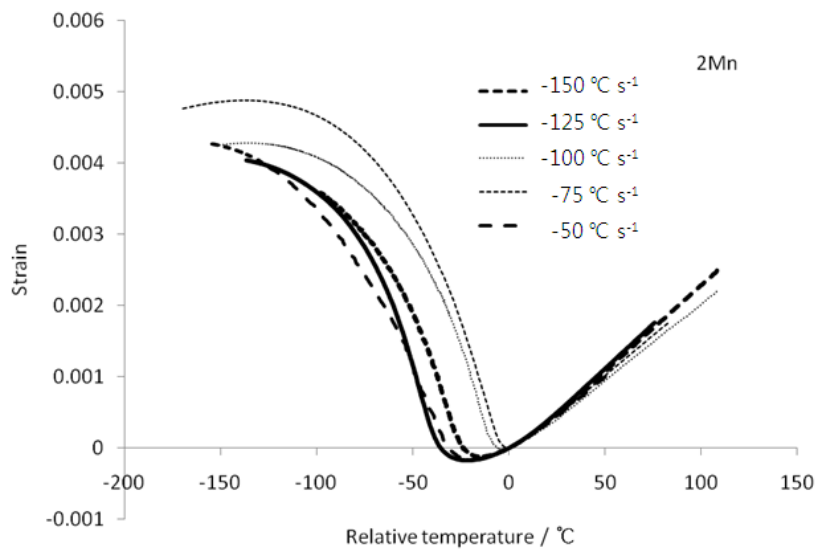


Fig. 3.9: Relative temperature- strain curves for the 2Mn alloy. At the origin, they have $T_S^{\gamma\alpha}$ temperatures.

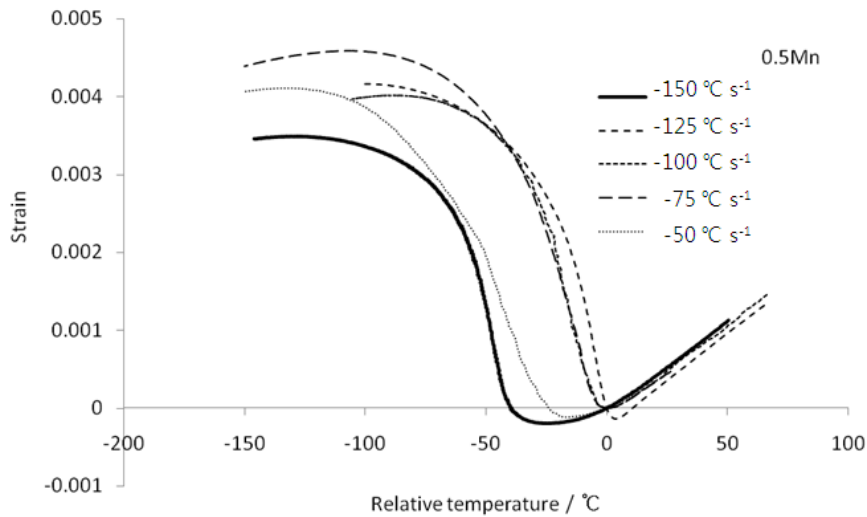


Fig. 3.10: Relative temperature-strain curves for the 0.5Mn alloy. At the origin, they have $T_S^{\gamma\alpha}$ temperatures.

3. Conclusions

The offset method was used to determine M_S temperature (Yang and Bhadeshia, 2007). The M_S of the 2Mn and 0.5Mn alloy was determined as $356\text{ °C} \pm 17\text{ °C}$ and $404\text{ °C} \pm 19\text{ °C}$, respectively. And it was suggested that the localization of certain solutes can cause the rate of transformation to be affected to give a high $T_S^{\gamma\alpha}$. The localization could also affect the scatter in hardness. These data will be used consequently in interpreting the development of coalesced bainite.

IV. Neural network modelling

The aim of the work presented in this chapter is to analyze the predictions of a neural network model for the impact toughness of weld metal and to study the underlying metallurgy. The first part of this work is a study of the influence of output forms on the mathematical behaviour of the trained function. Then the general performance of the created model is demonstrated. Finally the effect of selected input variables and interpass temperature had been studied and found to reveal interesting patterns.

1. Biased models

Since a neural network is a regression method, there is a risk of producing unphysical relationships. Yescas *et al.* (2001) used a combination of logarithms to avoid unphysical negative volume fractions. The double logarithm function in that work is consistent with Avrami theory (Bhadeshia, 2001), in which volume fraction, ξ varies as $\xi = 1 - \exp(-kt^n)$, so that $\ln[-\ln(1 - \xi)]$ should vary with $n \ln t$. Here k and n are constant and t is the time. The volume fraction is therefore naturally confined between 0 and 1.

At the beginning of this work, the following equation was similarly utilized to avoid predicting negative values of impact toughness:

$$y' = -\ln \left\{ -\ln \left(\frac{y - y_{min}}{y_{max} - y_{min}} \right) \right\} \quad (4.1)$$

where y is the impact toughness, y_{min} and y_{max} are the minimum and maximum set values of impact toughness. Compared with the original equation of Yescas, a minus sign was added to retain a direct proportionality between value of y and y' . The value of y_{min} was set as zero, the least

physical value of impact toughness. y_{max} must be larger than the maximum value in the dataset, but beyond that its magnitude could not be justified physically. Thus two different models were created. The y_{max} of the first model was set to the maximum value of impact toughness in database, 357 J and in the second model, it was arbitrarily set to ten times this value, at 3570 J. Some calculations using randomly selected inputs from the database (Table 4.1) are illustrated in Fig 4.1. Since the purpose was to highlight the influence of y_{max} , the extrapolation was performed to impractically high test temperature regimes. Note that any error bars of prediction by neural networks in this work include $\pm 1\sigma$ and fitting uncertainty as calculated by the Bayesian framework (MacKay, 1995).

Table 4.1 Base input conditions used for the neural network calculated to examine the influence of y_{max} . All elements are in wt% unless otherwise specified.

C	Si	Mn	S	P	Ni
0.034	0.27	2.14	0.008	0.01	7.3
Cr	Mo	V	Cu	Co	W
0.5	0.62	0.011	0.03	0.009	0.005
O/ppmw	Ti/ppmw	N/ppmw	B/ppmw	Nb/ppmw	
330	80	120	10	10	
HI/kJmm ⁻¹	IT/ °C	PWHTT/ °C	PWHTt/h	D _{Fe}	
1	250	20	0	0	

ppmw: Part per million by weight

HI: Heat input IT: Interpass temperature

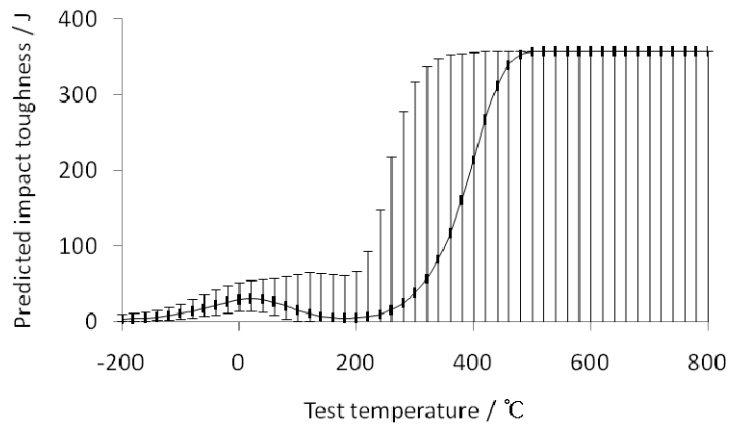
PWHTT: Post-weld heat treatment temperature

PWHTt: Post-weld heat treatment time

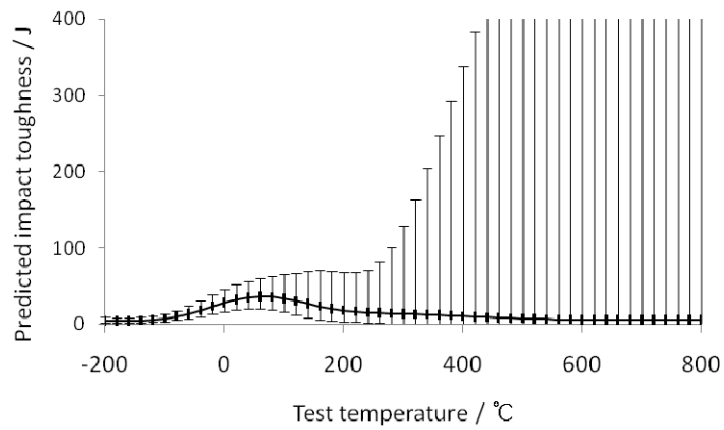
D_{Fe}: A variable considering iron diffusion during post-weld heat treatment

The extrapolated results in Fig. 4.1 are dramatically different. With the first model with $y_{max}=357$ J the limiting value at high temperature converges

artificially to y_{max} . However, for the model with $y_{max}=3570$ J the extrapolated maximum predicted value converges to nearly zero toughness.. This implies strongly that the selection of y_{max} plays a role in biasing during modelling or during the undoing of double logarithms in the final step to obtain toughness. The problem is that such a bias cannot be justified. Thus using equation 4.1 was abandoned. An alternative to use $y' = \ln y$ was also excluded because it practically allows an infinite value of y_{max} which cannot be justified either. In conclusion it was decided to use just the raw toughness values as the output in all the modelling and to be careful in interpreting the outputs.



(a) $y_{min}=0\text{J}$ and $y_{max}=357\text{J}$



(b) $y_{min}=0\text{J}$ and $y_{max}=3570\text{J}$

Fig. 4.1: Extrapolation results illustrating the influence of y_{max} on neural network prediction. The prediction results (b) are plotted to a maximum of 400J because of the huge value of the upper limits of uncertainty to a maximum of 1517J.

2. Interpass temperature

Lots of predictions were explored to attempt to discover significant phenomena worthy of careful study. Interesting relationships related with the interpass temperature were found, based on the input conditions listed in Table 4.2, extracted from Muruganath's work (2002). They practically correspond to the compositions of the 0.5Mn alloy and the 2Mn alloy of the present thesis.

Table 4.2 Base input condition used for the neural network prediction. All elements are in wt% unless otherwise specified (Muruganath, 2002).

C	Si	Mn	S	P	Ni
0.025	0.37	0.65/2	0.006	0.013	6.6
Cr	Mo	V	Cu	Co	W
0.21	0.4	0.011	0.03	0.009	0.005
O/ppmw	Ti/ppmw	N/ppmw	B/ppmw	Nb/ppmw	
380	80	180	1	10	
HI/kJmm ⁻¹	IT/ °C	PWHTT/ °C	PWHTt/h	D _{Fe}	TT/ °C
1	250	20	0	0	-60

The biggest physical effect of the interpass temperature during welding is to influence the cooling rate. This can be seen from the Rosenthal equation (Kurz, 1995):

$$T - T_0 = \frac{P}{2\pi\kappa r} \exp\left\{-\frac{v(\xi+r)}{2a}\right\} \quad (4.2)$$

where T is local temperature due to a point source of power input P moving at velocity v . T_0 is the far-field plate temperature which is equivalent to the interpass temperature in this case. κ is the thermal conductivity and a is the thermal diffusivity. r is a polar co-ordinate measured from a reference frame

attached to the moving heat source, related to the stationary frame by:

$$r = \sqrt{\xi^2 + y^2 + z^2} \quad (4.3)$$

where ξ is a coordinate measuring the translation of the heat source, y and z simply being coordinate axes orthogonal to ξ . Thus the cooling rate is expected to decrease as the interpass temperature increases (Lord, 1999).

This dependence of cooling rate on interpass temperature was confirmed by the simulating system devised by Svensson *et al.* (1986). Table 4.3 shows the cooling time between 800 °C and 500 °C for each interpass temperature. The calculation was performed with 180 A, 34 V and 0.004 m s⁻¹ for arc voltage, current and welding speed, respectively.

Table 4.3 Calculated cooling time between 800 °C and 500 °C ($t_{8/5}$) according to interpass temperature (Svensson *et al.*, 1986)

Interpass temperature (°C)	100	200	300	400
$t_{8/5}$ (s)	11.7	16.6	26.3	53.1

As interpass temperature increases, the cooling time increases further, which means drastic decrease of cooling rate. This matches well to the above theory.

Lord (1999) reported that in a continuous cooling transformation (CCT) diagram when the cooling curve of a weld metal crosses a C-shaped curve between M_s and B_s at which the gradient of C curve is large, the small variation of cooling rate by the uncontrolled interpass temperature can drastically alter the transformation temperature and thereby the resultant mechanical properties, especially the yield strength. The impact toughness, however, was in his work suggested to be insensitive to the interpass temperature in his concern.

3. General results of modelling

A total of 50 sub-models was produced using different combinations of hidden units and initial conditions for approaching the optimum weights. The maximum number of hidden units was confined to 10 in order to avoid an extensive computing time. Fig. 4.2 shows the evolution of the combined test error with an increasing number of members in a committee of models. With 19 sub-models, the combined test error was minimized.

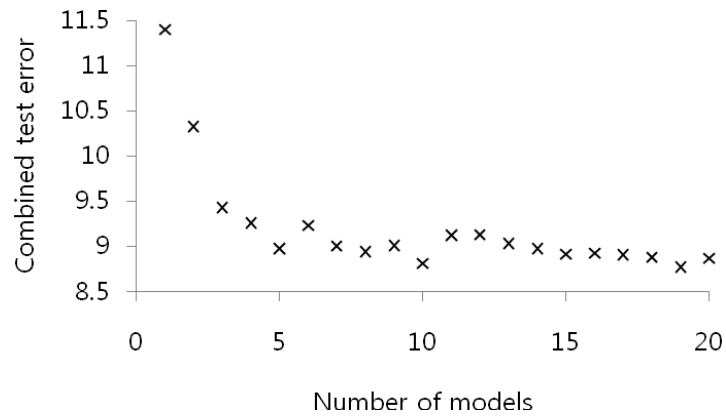


Fig. 4.2: The evolution of combined test error that was minimized with 19 sub-models.

Fig. 4.3 shows the perceived significances of each of the input variables of the best three models designated h4, i1 and h1. The significance of D_{Fe} calculated from the post-weld heat treatment temperature and time was as expected. It was unexpected that the significance of chromium is relatively high. It was therefore selected as one of the main variables in a later study.

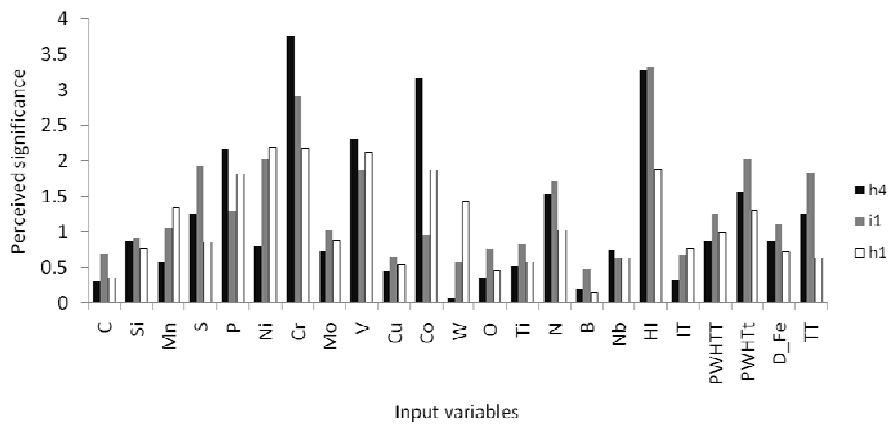
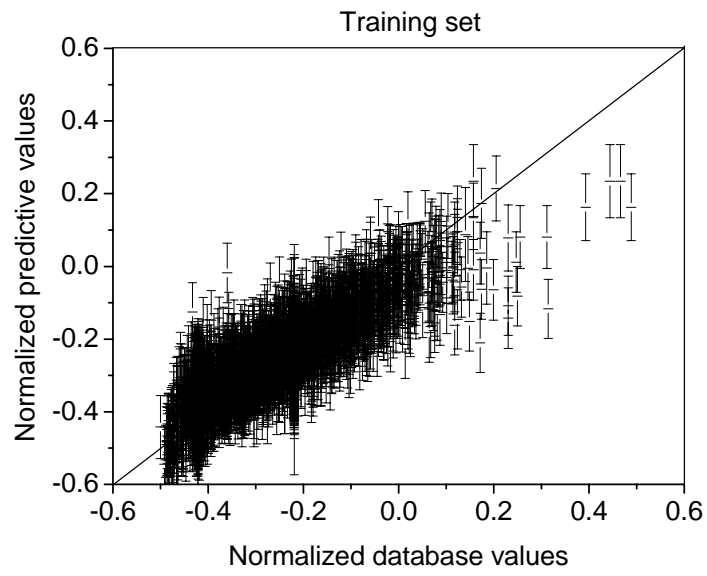


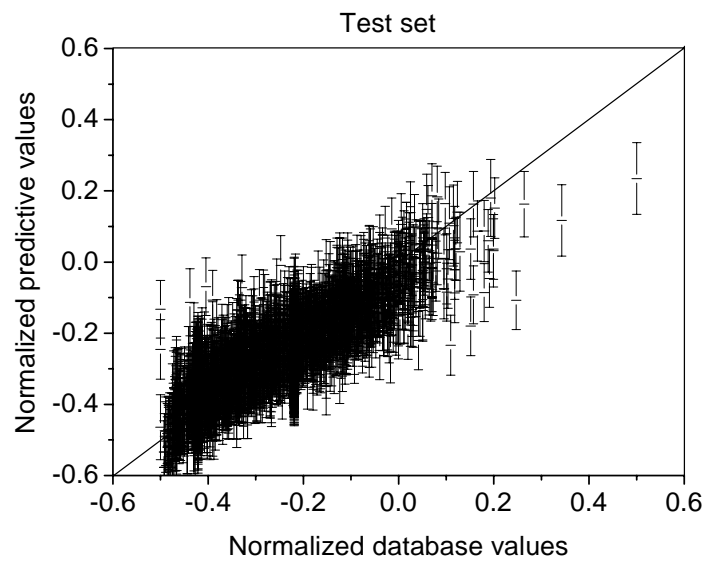
Fig. 4.3: Perceived significances of individual input variables

Finally the combined model was tested using the training and test data sets. The uncertainty in both predictions varied between 28 J and 48 J. Fig. 4.4 illustrates the results in their normalized values. The performance based on the test data does not differ critically from that of training data. This indicates that the training and test data were divided properly before creating a sub-model because a grouped dataset by related experiments can influence modelling through bias.

To avoid confusion from nomenclature, the term “a model” henceforth refers to the combined model rather than an individual sub-model.



(a) training set



(b) test set

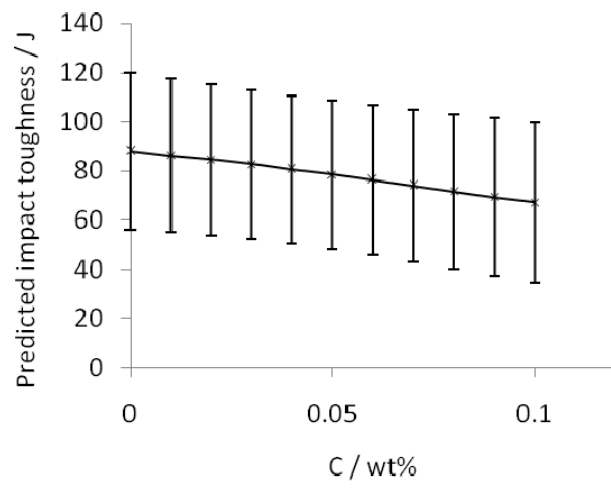
Fig. 4.4: Predicted and measured impact toughness

4. Results and analyses

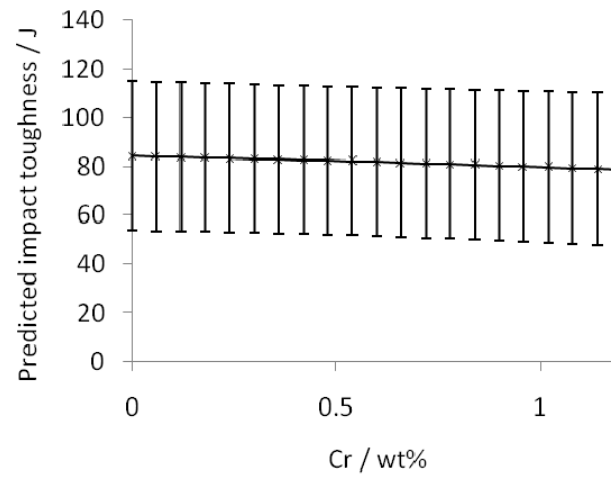
The influence of interpass temperature on impact toughness was studied as a function of another selected input variable, for example, carbon, chromium, manganese and nickel. Carbon is of course an important basic solute in the steel, chromium for its large perceived significance (Fig. 4.3) and nickel and manganese following Muruganath's work (2002).

4.1 Effects of individual input variables

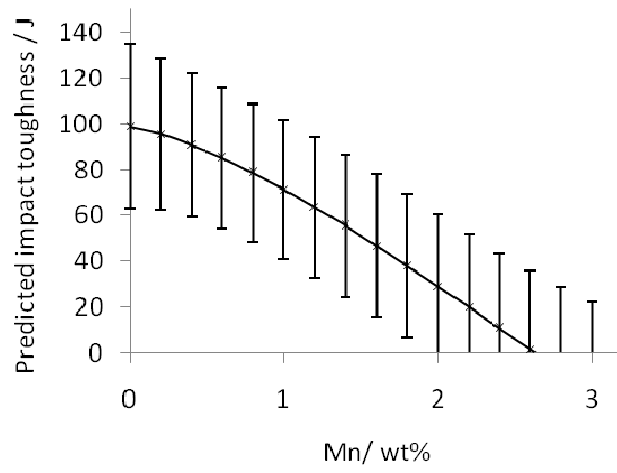
The effects of individual inputs on impact toughness were examined based on the 0.5Mn composition (Fig. 4.5). While the selected inputs varied, the other inputs were fixed to the values in Table. 4.2. As expected, increasing carbon reduced the impact toughness because of its hardening effects. Chromium doesn't affect as much as carbon in spite of its large significance. This emphasizes the fact that significance is a measure of correlation with the input rather than the sensitivity of the output to that variable, rather as the correlation coefficient in linear regression does not indicate the slope of the line. Manganese and nickel exhibited their outstanding sensitivity on impact toughness. Comparing carefully with the experimental results of Keehan *et al.* (2006b), good agreement was found about the effect of carbon, manganese and nickel.



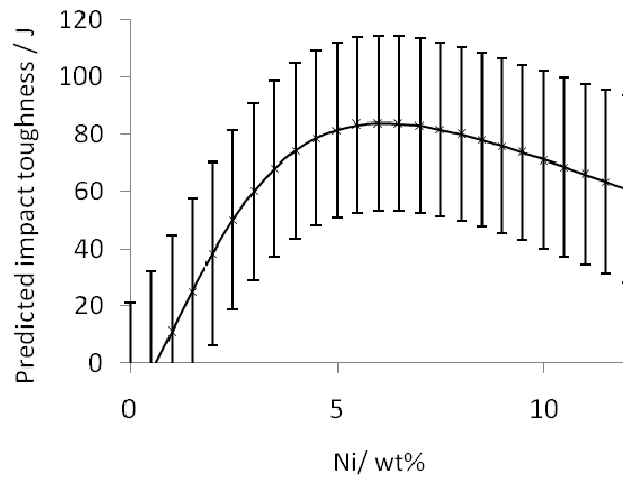
(a)



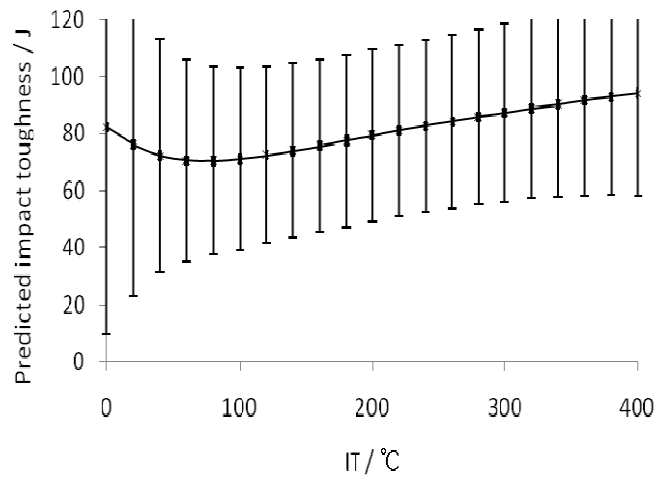
(b)



(c)



(d)



(e)

Fig. 4.5: Effect of individual inputs on impact toughness

Especially, the influence of interpass temperature was interesting. Increasing interpass temperature to around 80 °C deteriorated the impact toughness (Fig. 4.5(e)). Though the uncertainty is large at low interpass temperature, this trend corresponds to the result of Lord's work (1999) where the impact toughness with the interpass temperature, 99 °C was lower than that with 38 °C (Fig. 4.6).

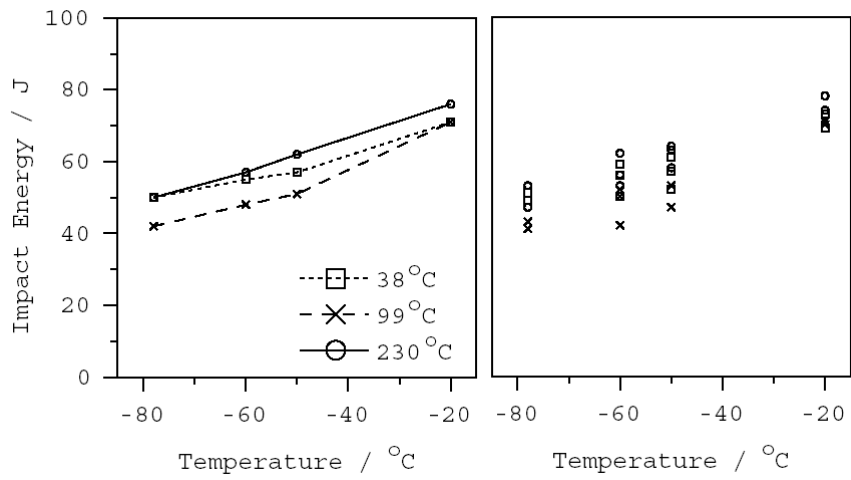


Fig. 4.6: Charpy impact data showing both average values (left) and scatter (right) (Lord, 1999).

As a precaution, in Fig. 4.7, the predictions based on the Lord's composition (Table 4.4) were compared with the results of based on Muruganath's work (Table 4.2). The compositions of unspecified chemical elements in Table 4.4 were used as the values in Table 4.2, however, the composition of oxygen was set to 300 ppmw as a general value for manual metal arc welding.

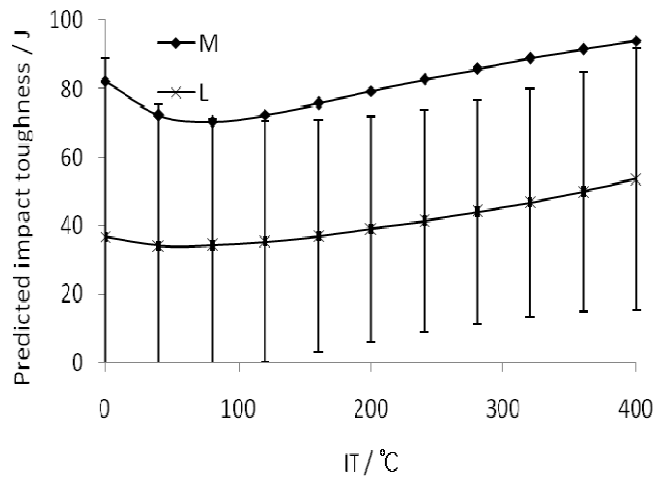


Fig. 4.7: Predictions based on Lord's composition

In Fig. 4.7 M and L represents the predictions based on Muruganath's and Lord's composition, respectively. Even though the predictions based on Lord's data have big uncertainties, they reflected the general behaviour of the experimental results of Fig. 4.6 and were consistent with the estimates based on Muruganath's composition. Thus the predictions by created model, especially about interpass temperature, were found to be reliable.

Table 4.4 Chemical composition in Lord's experiments (wt%) (Lord, 1999).

C	Si	Mn	Ni	Cr	Mo	Cu
0.05	0.30	2.0	3.0	0.45	0.6	0.0

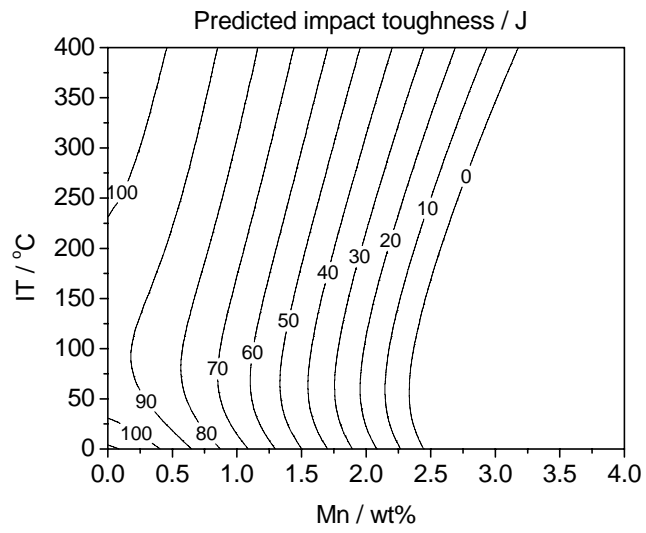
4.2 Influence of interpass temperature

The influence of interpass temperature with the selected variables was studied further by analyzing contour plots for predicted impact toughness. The predictions were done using the listing in Table 4.2. In each prediction, while two of the variables were varied, the others were fixed at values listed in Table.4.2.

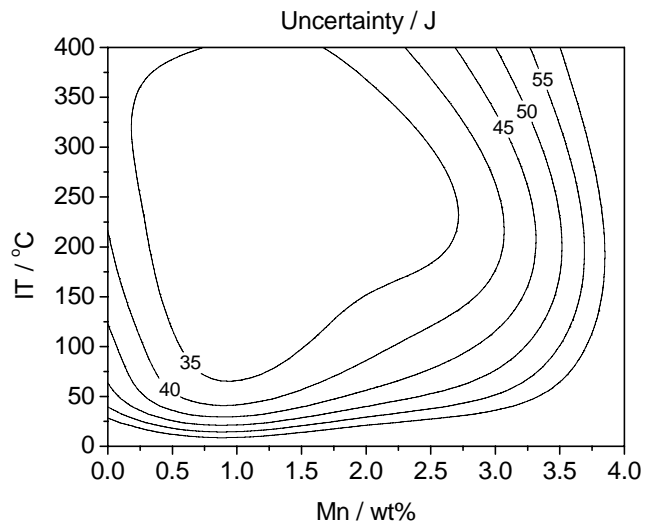
4.2.1 Manganese

In Fig. 4.8, the reduction of impact toughness by increasing the interpass temperature was observed in the low interpass temperature region, as expected in Fig. 4.5(e). This was common in the predictions with other variables.

The sensitivity of the impact toughness to the interpass temperature at 2 wt% Mn was higher than that at 0.5 wt% Mn, however, it should be noticed that the uncertainties at high manganese concentration exceeded the variation of the impact toughness.



(a)



(b)

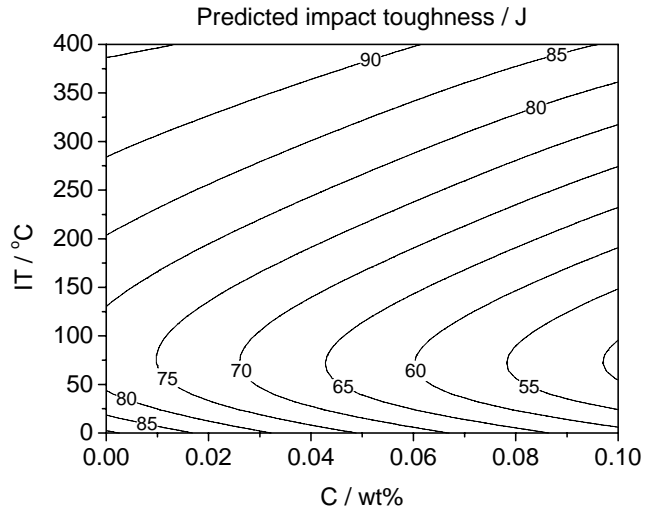
Fig. 4.8: Influence of interpass temperature and manganese on the impact toughness. (a) Predicted impact toughness. (b) Uncertainty ($\pm 1\sigma$)

4.2.2 Carbon and chromium

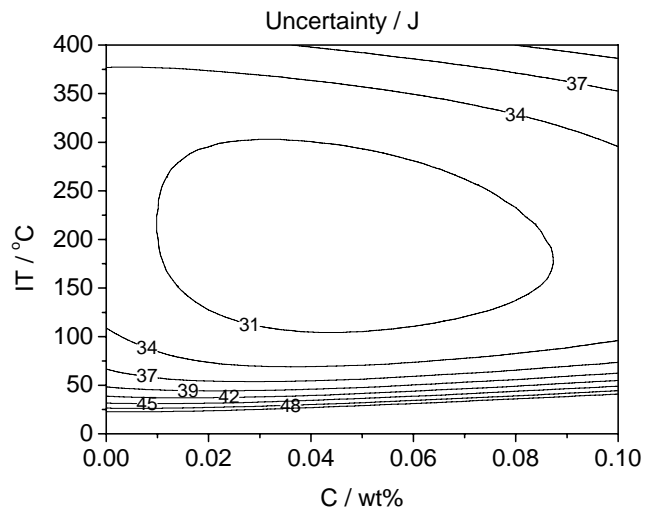
Interpass temperature influenced the impact toughness in a similar way for carbon and chromium. Figs. 4.9 and 4.10 show the combined effects of interpass temperature with two elements based on the 0.5Mn composition. As already mentioned in the case of manganese, the increase at low interpass temperature caused a deterioration of the impact toughness. Except for that region, increasing interpass temperature enhanced impact toughness over the whole range of composition considered.

It is particularly noticeable that for both cases, the contour plots in the diagram are quite parallel. This implies that the interpass temperature interacts with carbon and chromium in a consistent way.

Same analyses were applied to the plots based on the 2Mn composition. Figs. 4.11 and 4.12 are the plots for carbon and chromium, respectively. As expected they were not much different with those of the 0.5Mn composition except for absolute value of impact toughness. However the small impact toughness values of the 2Mn alloy was already expected from the work of Keehan *et al.* (2006b).

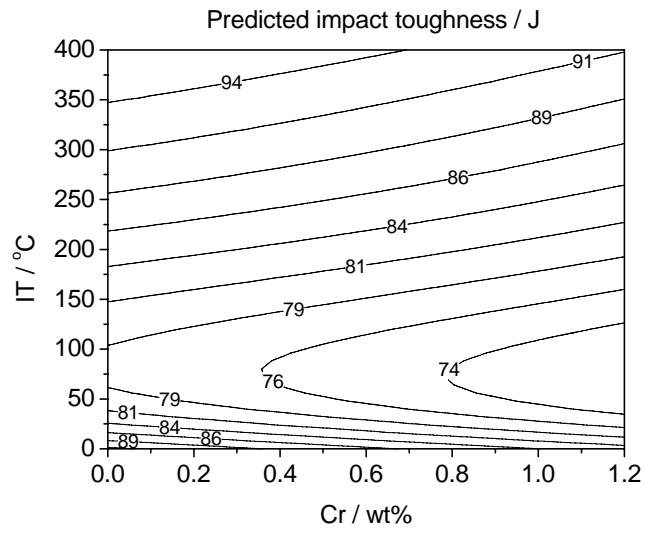


(a)

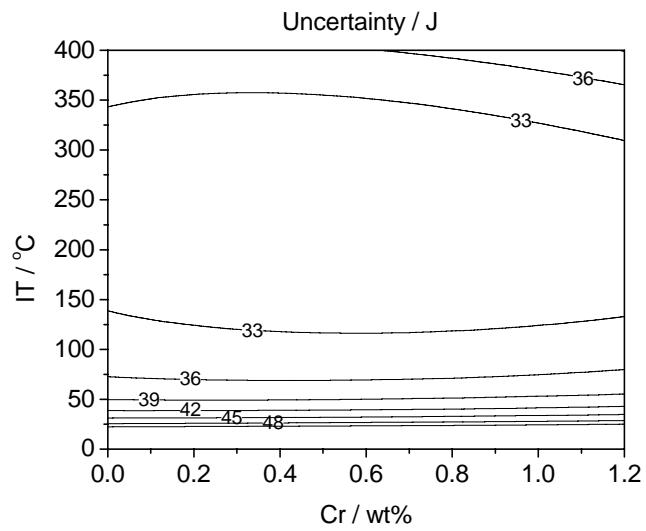


(b)

Fig. 4.9: Influence of interpass temperature and carbon on the impact toughness of the 0.5Mn composition. (a) Predicted impact toughness. (b) Uncertainty ($\pm 1\sigma$)

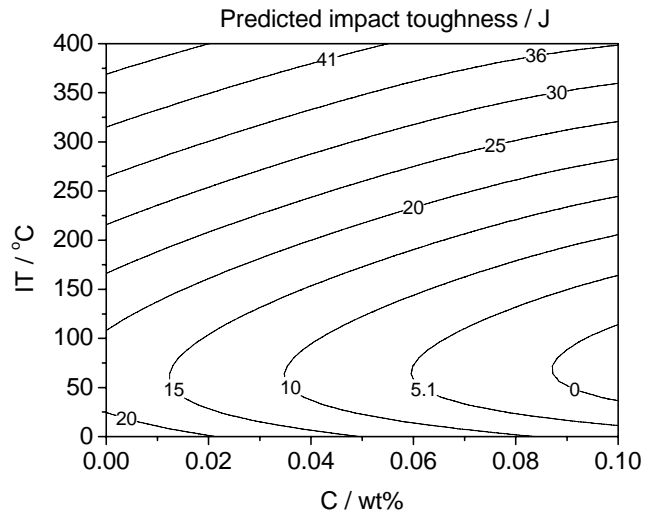


(a)

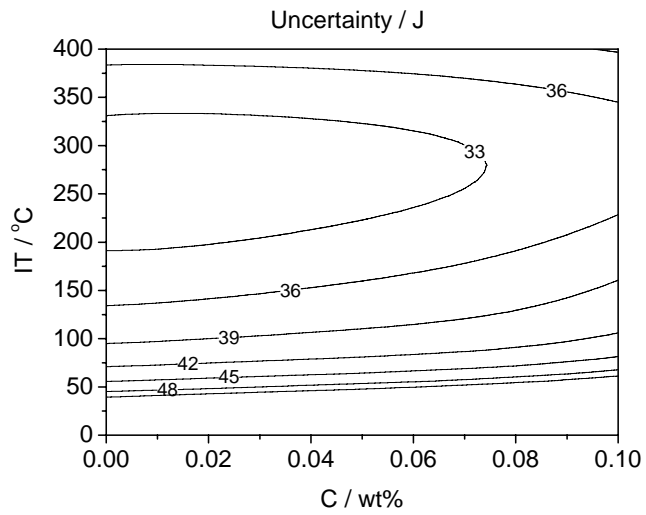


(b)

Fig. 4.10: Influence of interpass temperature and chromium on the impact toughness of the 0.5Mn composition. (a) Predicted impact toughness. (b) Uncertainty ($\pm 1\sigma$)

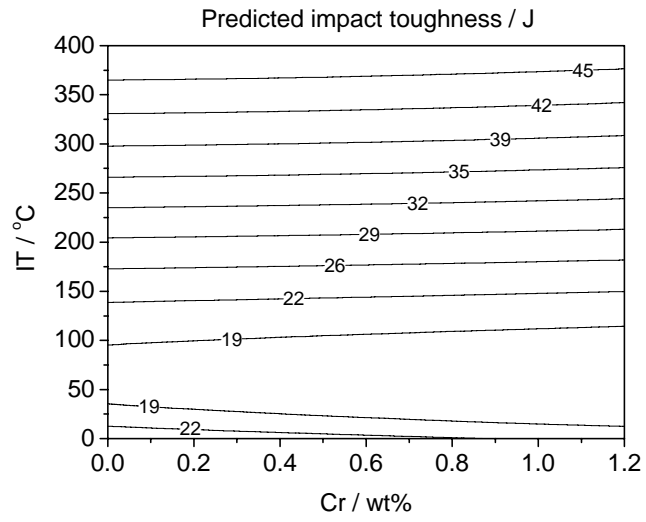


(a)

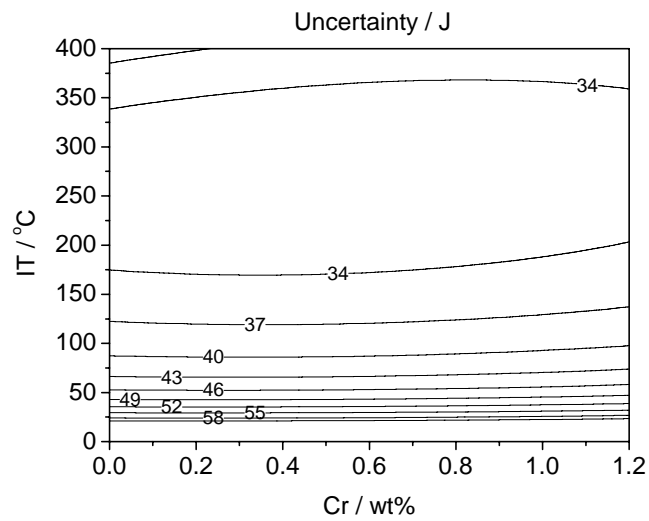


(b)

Fig. 4.11: Influence of interpass temperature and carbon on the impact toughness of the 0.5Mn composition. (a) Predicted impact toughness. (b) Uncertainty ($\pm 1\sigma$)



(a)



(b)

Fig. 4.12: Influence of interpass temperature and chromium on impact toughness of the 2Mn composition. (a) Predicted impact toughness. (b) Uncertainty ($\pm 1\sigma$)

4.2.3 Nickel

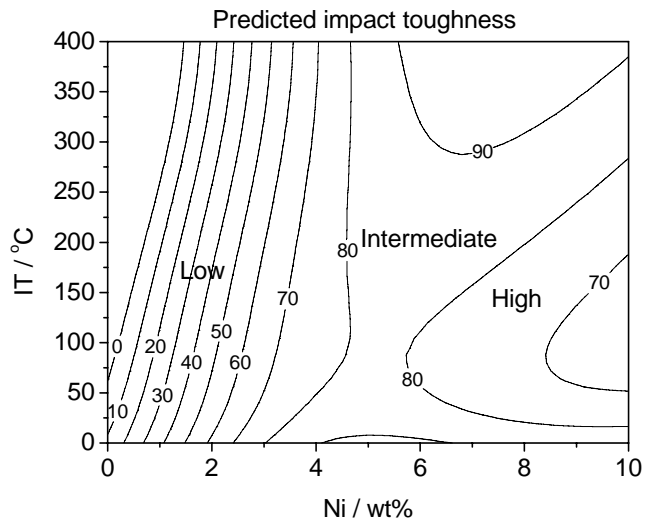
The most interesting features were observed in the nickel versus interpass temperature plots. The overall patterns of behaviour of interpass temperature in the prediction for the 0.5Mn and the 2Mn composition looked similar, but there were subtle differences.

The plot for the low nickel region of the 0.5Mn alloy is sensitive to the nickel concentration. Therefore, increasing the interpass temperature produced quite a large reduction in the impact toughness.

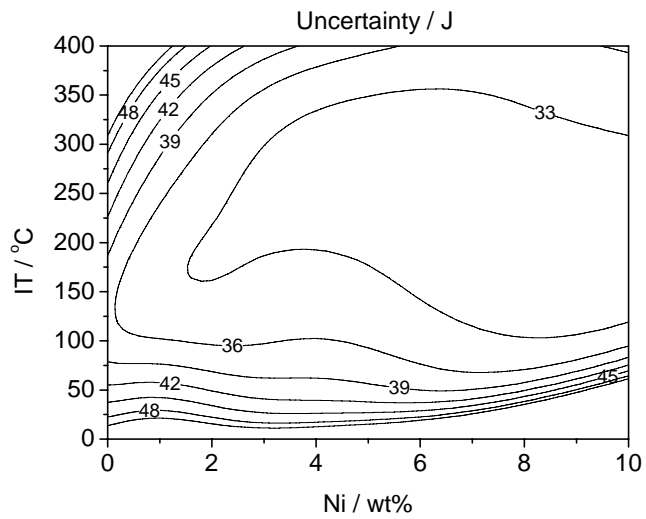
For nickel in excess of 6 wt%, increasing the interpass temperature improved the impact toughness, however, it was less effective compared with the variation at low nickel. This explains that at high solute concentrations, the microstructure of the weld becomes less sensitive to the cooling rate.

In the intermediate region, around 5 wt%, the impact toughness was not influenced by interpass temperature and nickel, becoming stable at a relatively high value. These three regions can be distinguished roughly as marked on Fig. 4.13 (a).

The plot based on the 2Mn composition also showed the characteristic features but the intermediate region was shifted to lower concentrations (Fig. 4.14). This is expected since the high concentration of manganese enhances the hardenability of the alloy and hence the role of interpass temperature diminishes.

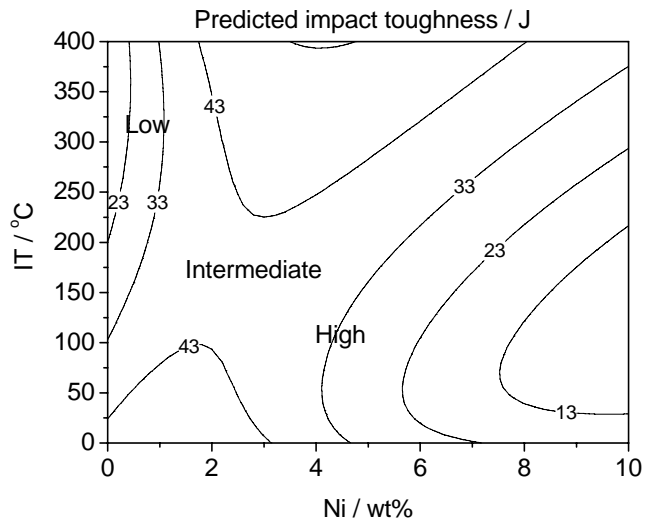


(a)

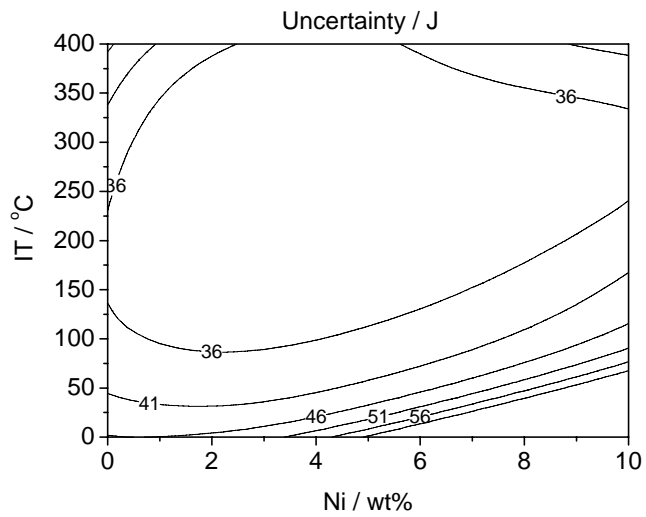


(b)

Fig. 4.13: Influence of the interpass temperature and nickel on the impact toughness of the 0.5Mn composition. (a) Predicted impact toughness. (b) Uncertainty ($\pm 1\sigma$)



(a)



(b)

Fig. 4.14: Influence of interpass temperature and nickel on the impact toughness of the 2Mn composition. (a) Predicted impact toughness. (b) Uncertainty ($\pm 1\sigma$)

5. Discussion

The enhancement of impact toughness by increasing interpass temperature is probably due to the evolution of softer microstructures which are encouraged to form at low cooling rates. This could be applied to almost all the situations studied. Some contradictions to this general behaviour were also observed. For example, increasing interpass temperature to around 80 °C led to a deterioration of impact toughness. In spite of big uncertainties with the predictions, this is worthy of further investigation with the experimental results of Fig. 4.6 as evidence. Using microscopy and hardness data would be useful in this context. If the prediction is true, it implies the existence of hard but not brittle structures.

Assuming that the variation of mechanical properties comes from the C-curve behaviour as reported by Lord (1999), the unique dependence of interpass temperature on the nickel content is interesting since adding carbon, chromium and nickel commonly retard the transformation of austenite (Bhadeshia, 2001).

The explanation about nickel-interpass temperature plots (Figs. 4.13 and 4.14), nevertheless, was tried in Fig. 4.15, where the solid lines are transformation curves and the dotted lines are cooling curves. With the low manganese composition (0.5Mn), the larger sensitivity of impact toughness at low nickel concentration can be explained by the variation of transformation temperature on the C-shape curve. On the other hand the relative insensitivity at high nickel corresponds to the invariance of transformation temperature. Adding manganese (2Mn) causes an increase of hardenability, thus pushing the transformation curve to longer times. This exactly corresponds to the shift of characteristic regions of the 0.5Mn nickel-interpass temperature plot to lower nickel.

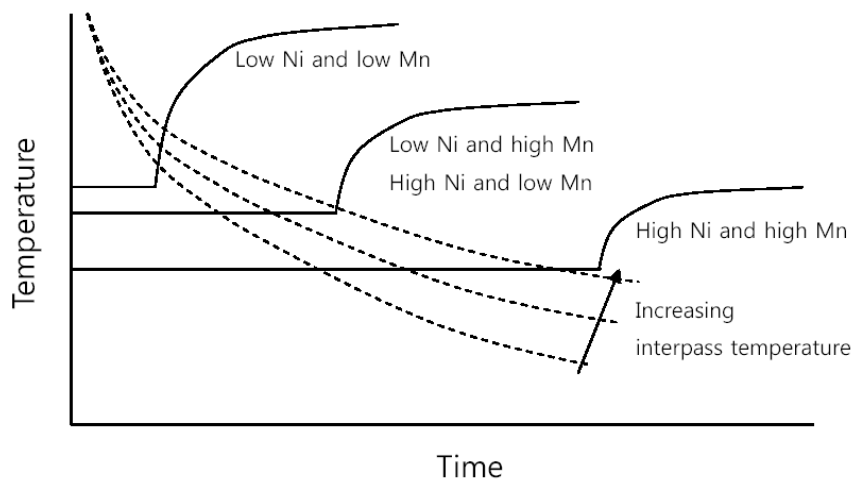
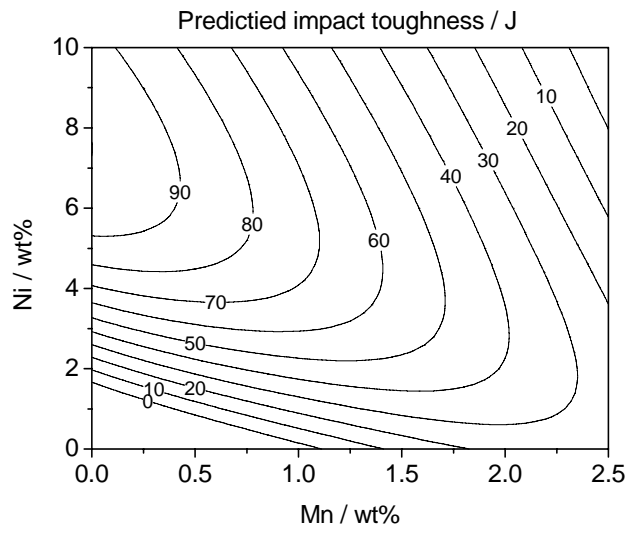
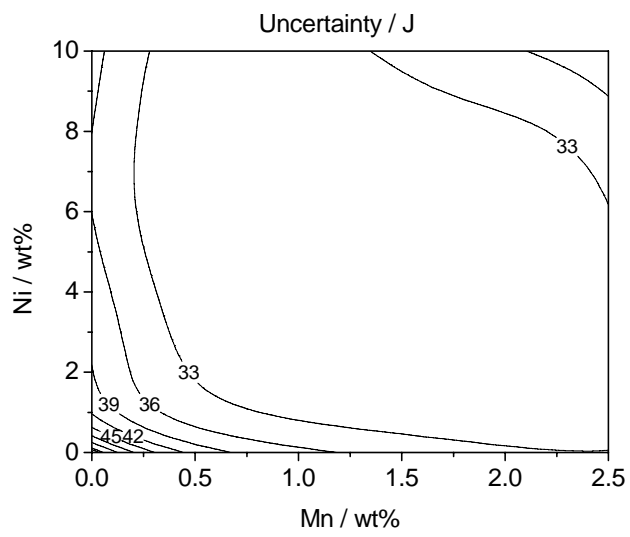


Fig. 4.15: Schematic diagram illustrating the effect of alloying solutes and interpass temperature on transformation temperature.

Actually, such a shift could be expected from the interaction of nickel-manganese in Fig. 4.16, where it shows that the high impact toughness can be obtained by the combination of low nickel and high manganese (2 wt% Mn) or high nickel and low manganese (0.5 wt% Mn). This corresponds to the shift of intermediate region to left comparing Fig. 4.14 with Fig. 4.13.



(a)



(b)

Fig. 4.16: Influence of manganese and nickel on the impact toughness (a) Predicted impact toughness. (b) Uncertainty ($\pm 1\sigma$)

6. Conclusions

It was discovered that double logarithms used to represent and bound the output form leads to unjustified bias in the modelling, so this method was not used in this work. Increasing interpass temperature can reduce impact toughness in some conditions. It is interesting that unique domains were identified in the nickel-interpass temperature plots, which were not typical in similar plots involving carbon, chromium and manganese.

V. Coalesced bainite

The main aim of the work presented in this chapter is to develop an understanding of the formation of coalesced bainite. Isothermal transformations were conducted at several temperatures above M_s to generate coalesced bainite in reheated weld deposits. The B_S temperatures of each alloy sample were measured from dilatometric data to study the effect of the difference between B_S and M_S as reported (Keehan *et al.*, 2006a).

1. The bainite-start temperature

The growth of bainite requires that the transformation occurs at a temperature below T_0 , when the free energy of bainite becomes equal to that of austenite of the same composition (Bhadeshia, 2001). Thus its growth can only occur if the carbon concentration of the austenite lies to the left of the T_0 curve on a plot of temperature versus carbon concentration. Since bainite formation involves the partitioning of carbon into the retained austenite following diffusionless growth, when the carbon concentration of austenite reaches the T_0 curve, the reaction stops. Fig. 5.1 illustrates that the amount of carbon that can be tolerated by the austenite before the bainite reaction stops, increases as the temperature decreases.

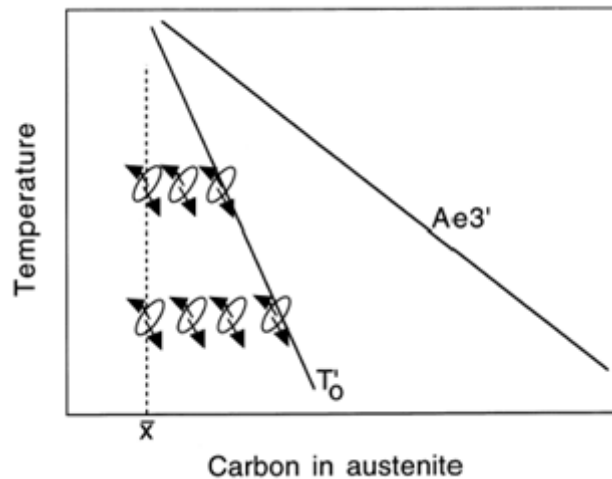
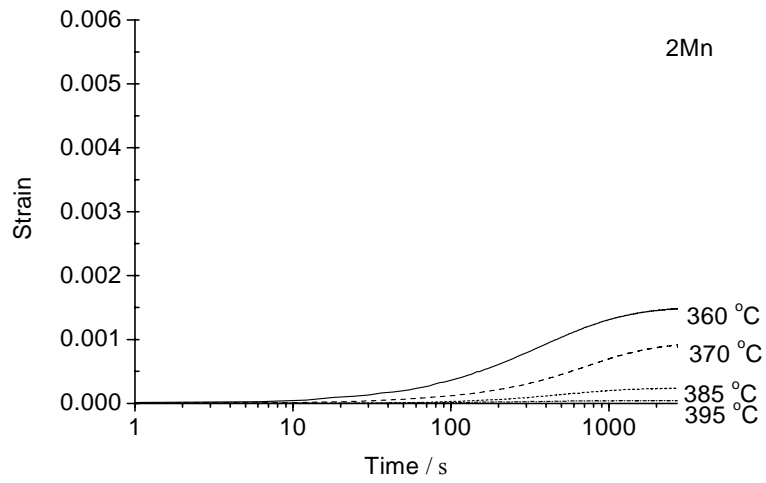


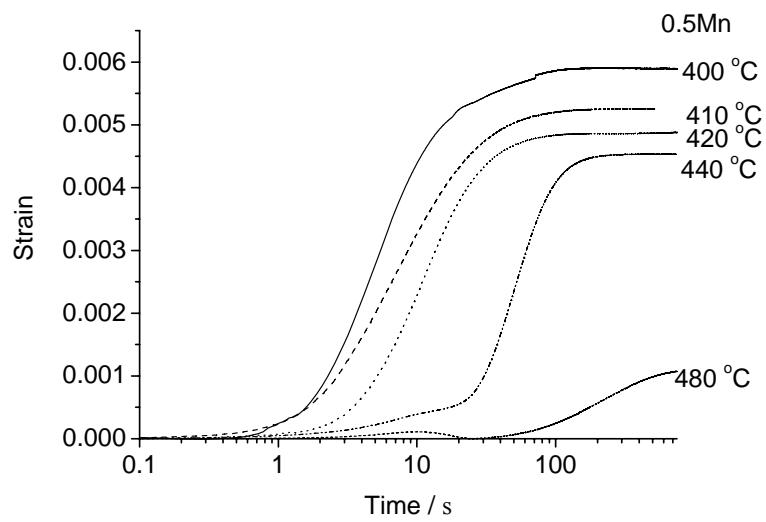
Fig. 5.1: Schematic diagram illustrating the degree of bainite transformation as temperature decreases. \bar{x} is the average carbon concentration of the state, T'_0 is the T_0 curve adjusted for the stored energy of bainite and $Ae3'$ is the $\alpha + \gamma/\gamma$ paraequilibrium phase boundary (Bhadeshia, 2001).

Since the total amount of partitioned carbon is related with the degree of transformation to bainite, greater undercoolings allow more bainite to form. In other words, the temperature where no transformation occurs corresponds to the bainite-start temperature (B_S). The overall phenomenon just described is known as the “incomplete reaction phenomenon”. The reaction stops before paraequilibrium is reached (Bhadeshia, 2001).

In the present work, the degree of transformation to bainite was measured using dilatometry. As expected, Fig. 5.2 shows that strain due to transformation increased as the transformation temperature is reduced. This, of course, is consistent with the incomplete reaction phenomenon. The retardation of transformation in high manganese sample due to the corresponding increase in the stability of the austenite was also confirmed.



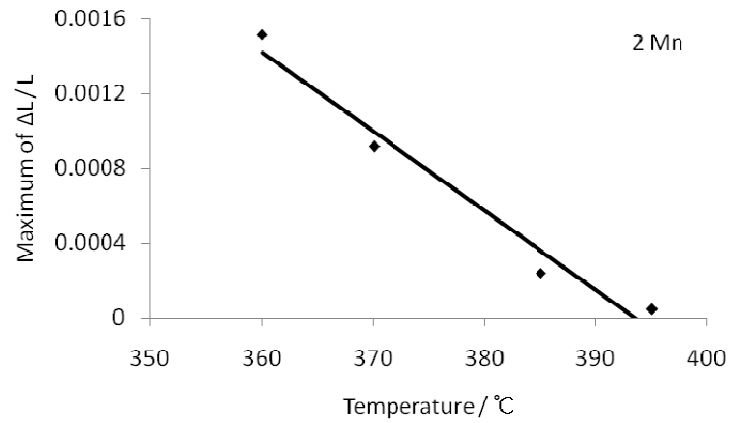
(a)



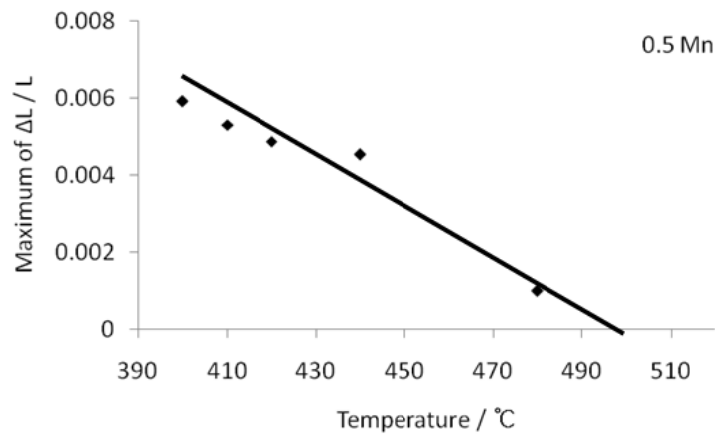
(b)

Fig. 5.2: Length changes observed during isothermal transformation at a variety of temperatures (a) the 2Mn alloy (b) the 0.5Mn alloy. Notice that the reaction is much slower with the 2Mn alloy.

Assuming that the maximum length change depends linearly on undercooling as illustrated in Fig. 5.1, the B_S temperatures were estimated as illustrated in Fig. 5.3.



(a)



(b)

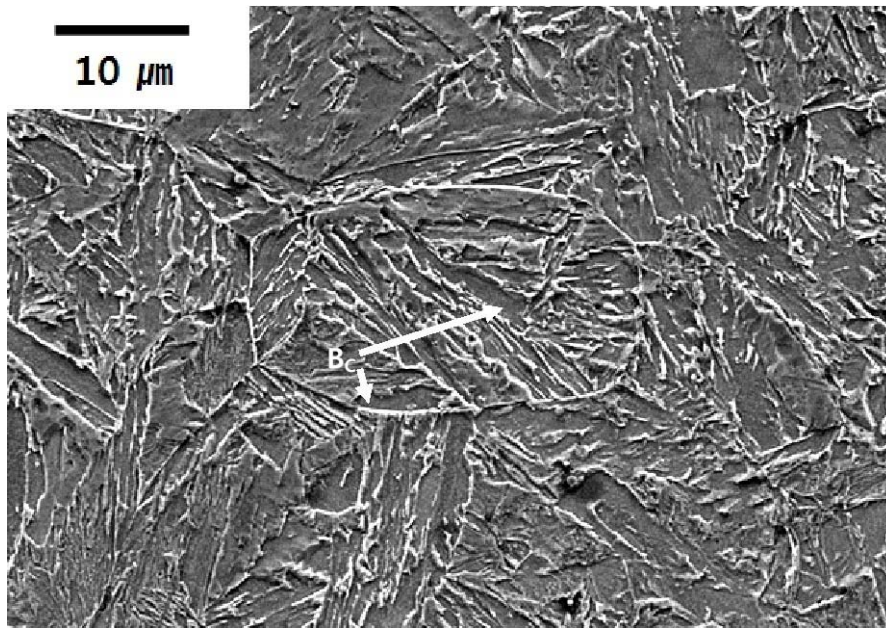
Fig. 5.3: Estimation of B_S of each alloy (a) the 2Mn alloy (b) the 0.5Mn alloy. $\Delta L/L$ is the measured transformation strain.

The B_S temperature was estimated as $393 \text{ }^\circ\text{C} \pm 11.1 \text{ }^\circ\text{C}$ for the 2Mn alloy and as $498 \text{ }^\circ\text{C} \pm 33.8 \text{ }^\circ\text{C}$ for the 0.5Mn alloy with 95% confidence.

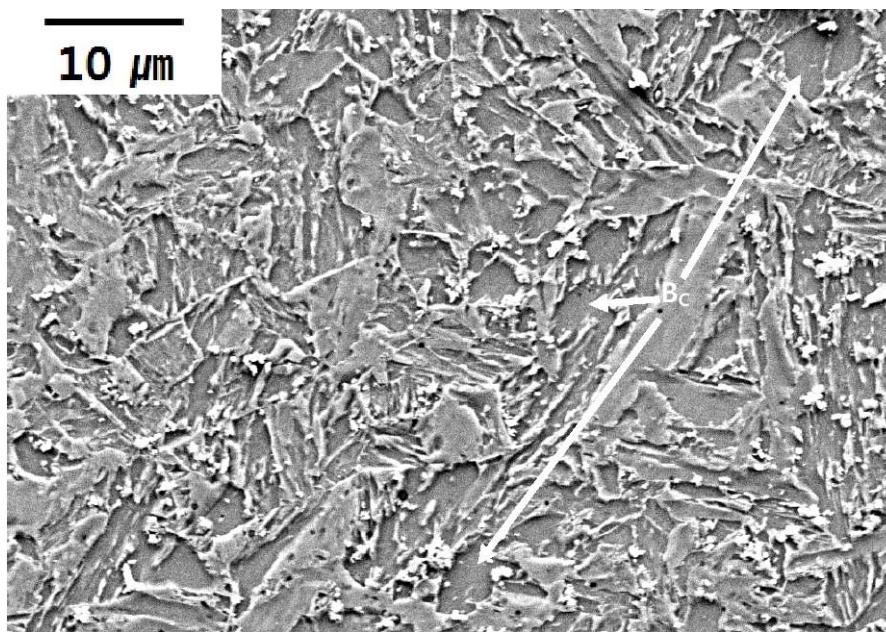
2. Coalesced bainite

2.1 The 2Mn alloy

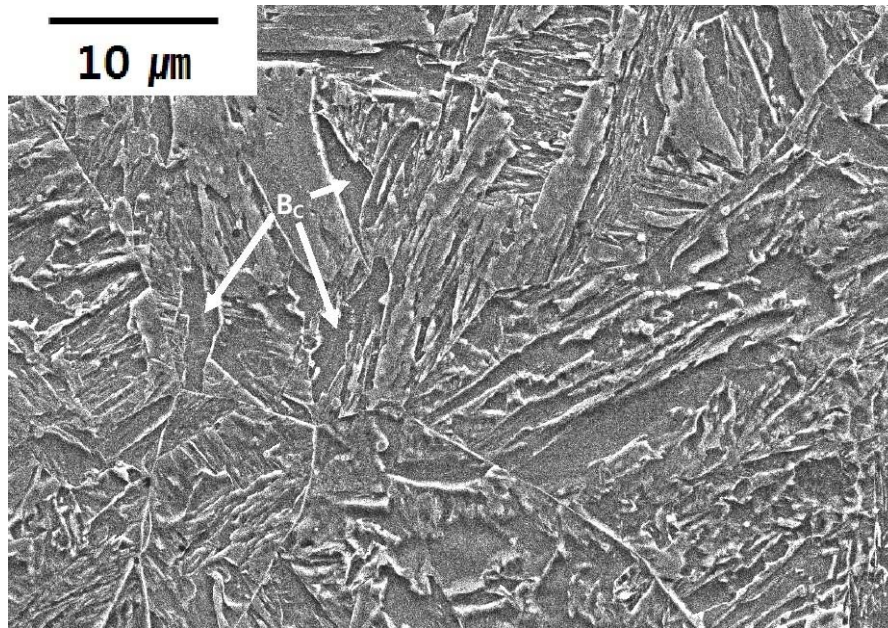
Field emission gun scanning electron microscopy (FEGSEM) was used to identify and characterize the microstructures, with a particular emphasis on the so-called coalesced bainite. Fig. 5.4 shows the FEGSEM micrographs of the 2Mn alloy samples which were transformed at 360, 370, 385 and 395 °C, respectively. The 'B_C' in the micrographs represents coalesced bainite and the temperature and time under each micrograph correspond to the set temperature and time.



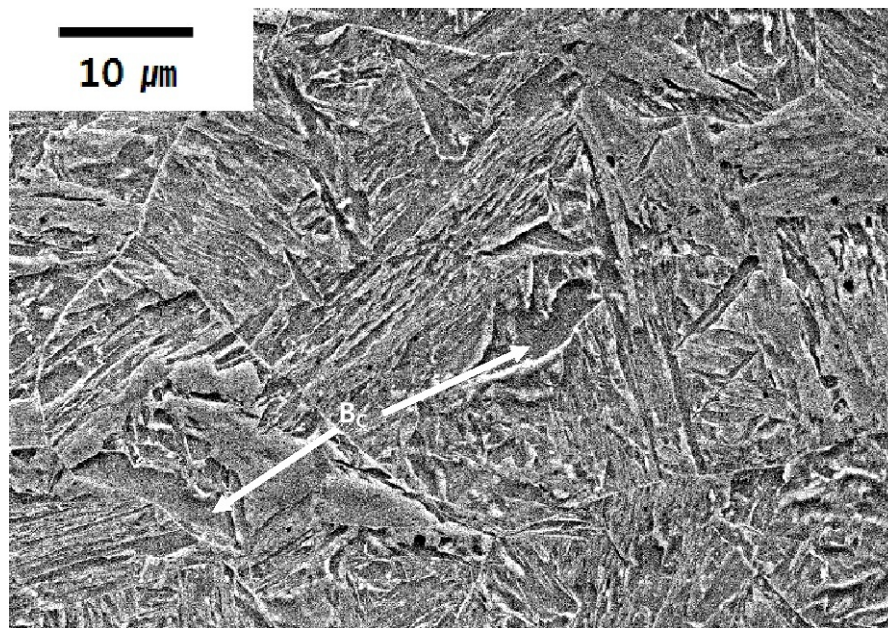
(a) 360 °C 1 h



(b) 370 °C 45 min



(c) 385 °C 3 h



(d) 395 °C 7 h

Fig. 5.4: FESEM micrographs of coalesced bainite formed at different temperatures in the 2Mn alloy

Coalesced constituents were observed at all temperatures and their morphology corresponds with that reported in the literature (Keehan, 2006a). Thus the marked constituents in each micrograph were identified as coalesced bainite. The overall views of each micrograph indicate that as the temperature increases, the occupancy by the characteristic “indented” regions associated with coalesced bainite decreases. Thus coalescence is likely to be suppressed at high temperatures.

It is noticeable that coalesced bainite was observed not only at the austenite grain boundaries but also inside the grains, probably nucleated from nonmetallic particles present in the weld deposit (Fig. 5.4 (a), (d)).

There was an interesting results observed by chance. During an isothermal transformation experiment at 370 °C, the dilatometer switched off suddenly. Fig. 5.5 is the incomplete length change curve from that experiment. It doesn't show a full S-curve and comparing the scale of time and length change with those of Fig. 5.2, the experiment stopped at a very early stage of transformation. It is surprising that the coalesced bainite was also found in this sample (Fig. 5.6). This supports the hypothesis by Chang and Bhadeshia (1996), which is that coalesced bainite forms at the early stages of transformation. However, the forming of coalesced bainite would be expected to continue because the overall degree of coalescence was low compared with that of Fig. 5.4(b).

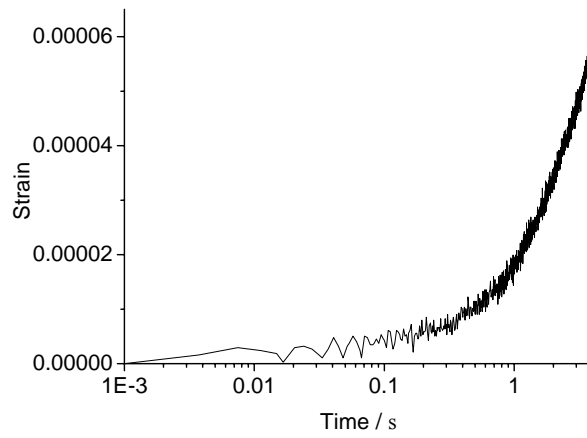


Fig. 5.5: Incomplete length change curve by isothermal transformation at 370 °C

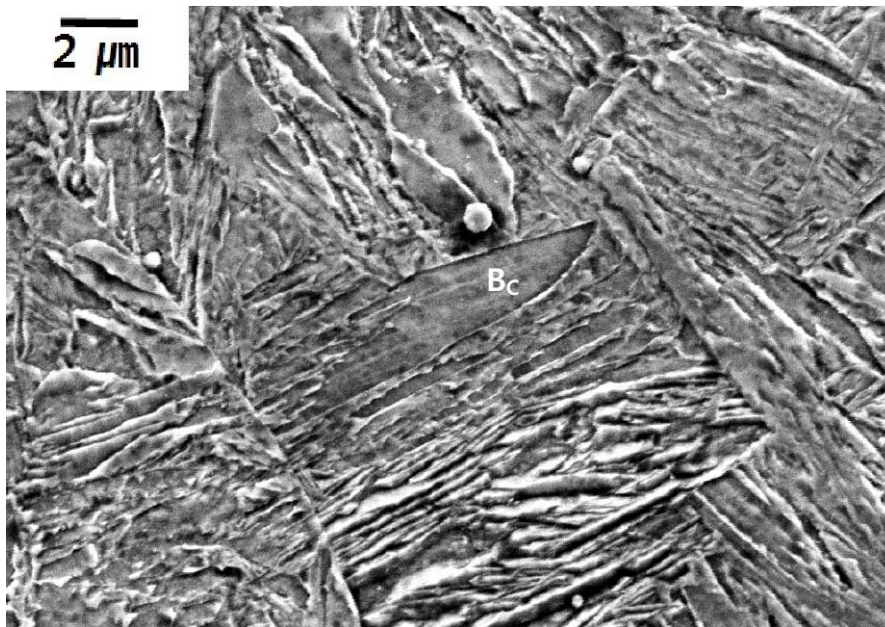


Fig. 5.6: Coalesced bainite formed by incomplete isothermal transformation at 370 °C in the 2Mn alloy

2.2 The 0.5Mn alloy

The FEGSEM micrographs of samples transformed at 380, 390 and 400 °C were studied. Those for the other temperatures will be obtained in the future. It should be interesting to compare the microstructures formed at 360 °C for the 2Mn alloy with those formed at 480 °C for the 0.5Mn alloy since they have comparable maximum length change (Fig. 5.2), corresponding to a similar driving force for transformation.

The isothermal transformation at 380 °C was found not to be truly isothermal. In normal isothermal transformation, the rate at which the length changes as a function of temperature should be constant during the cooling of austenite. However, that curve in Fig. 5.7 exhibited an additional length change before the required temperature of 380 °C was reached. Using the offset method (Yang and Bhadeshia, 2007), the transformation was found to begin at $422 \text{ °C} \pm 1 \text{ °C}$. Since this temperature is between the M_S ($404 \text{ °C} \pm 19 \text{ °C}$) and B_S ($498 \text{ °C} \pm 33.8 \text{ °C}$) of the 0.5Mn alloy, the unintended reaction corresponds to bainite formation. One interesting thing is that the coalesced bainite is also observed in this sample (Fig. 5.8). It is not certain that this coalesced bainite formed at 422 °C; however, the circumstances are favourable for the development of coalesced bainite because the driving force increases as the sample cools further toward M_S , making it likely that coalescence occurs.

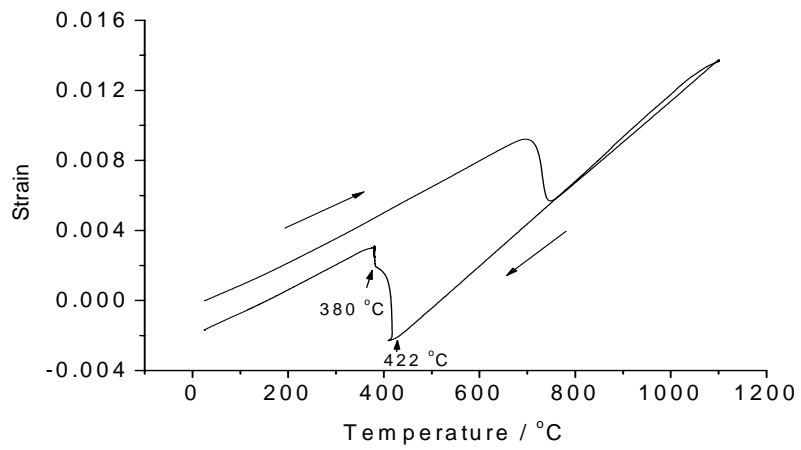


Fig. 5.7: Dilatometric curve designed for isothermal transformation at 380 °C

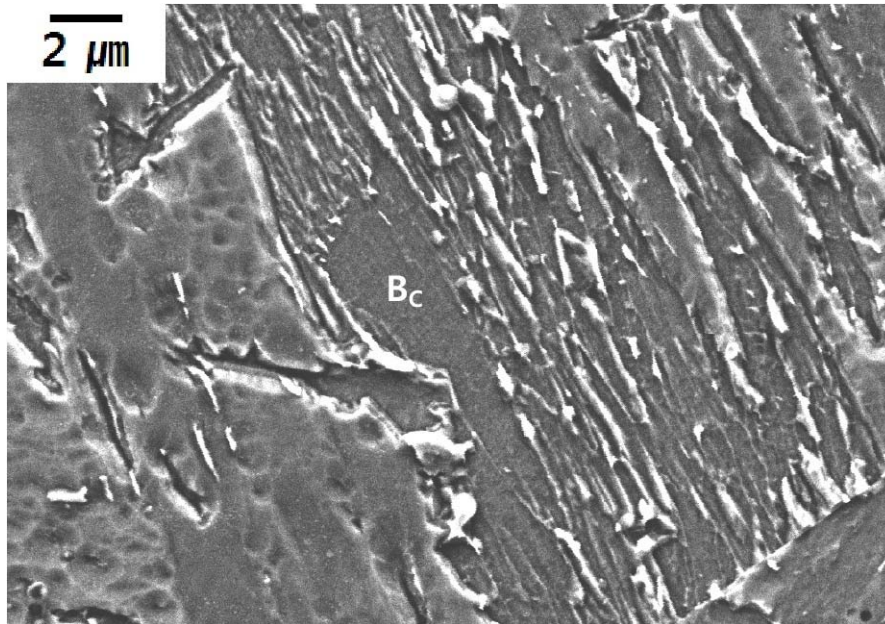


Fig. 5.8: Coalesced bainite in a sample designed for isothermal transformation at 380 °C in the 0.5Mn alloy. However, some transformation preceded the set temperature.

Coalesced bainite was also found in a sample (Fig. 5.10) which was designed for isothermal transformation at 390 °C however, the experiment was stopped before the maximum length change was obtained (Fig. 5.9) so their data are excluded from Fig. 5.2(b).

Fig. 5.10, nevertheless, indicates important facts about the evolution of coalesced bainite. Metallography showed various arrangements of coalesced bainite forming from the merger of parallel plates (Fig. 5.10).

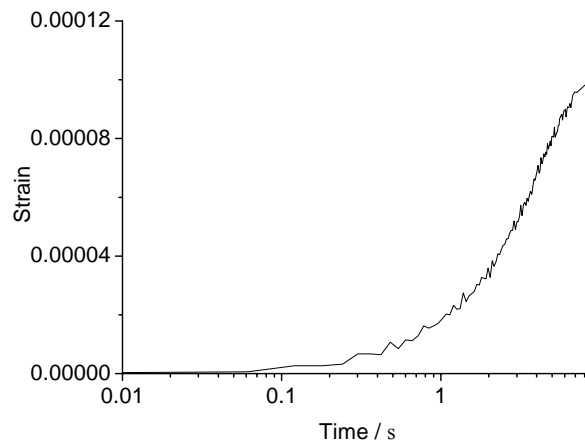


Fig. 5.9: Incomplete length change curve by isothermal transformation at 390 °C.

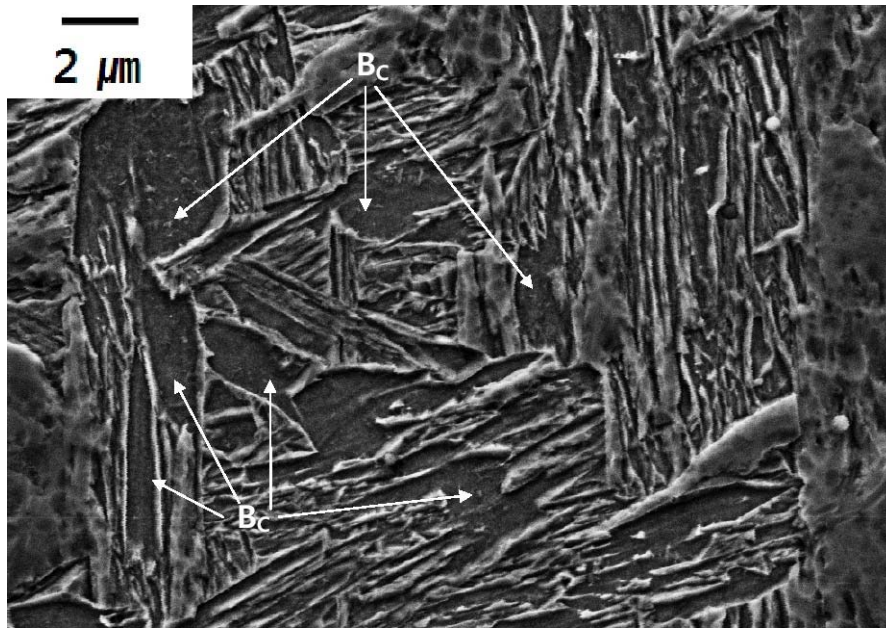


Fig. 5.10: Coalesced bainite in a sample designed for isothermal transformation at 390 °C in the 0.5Mn alloy.

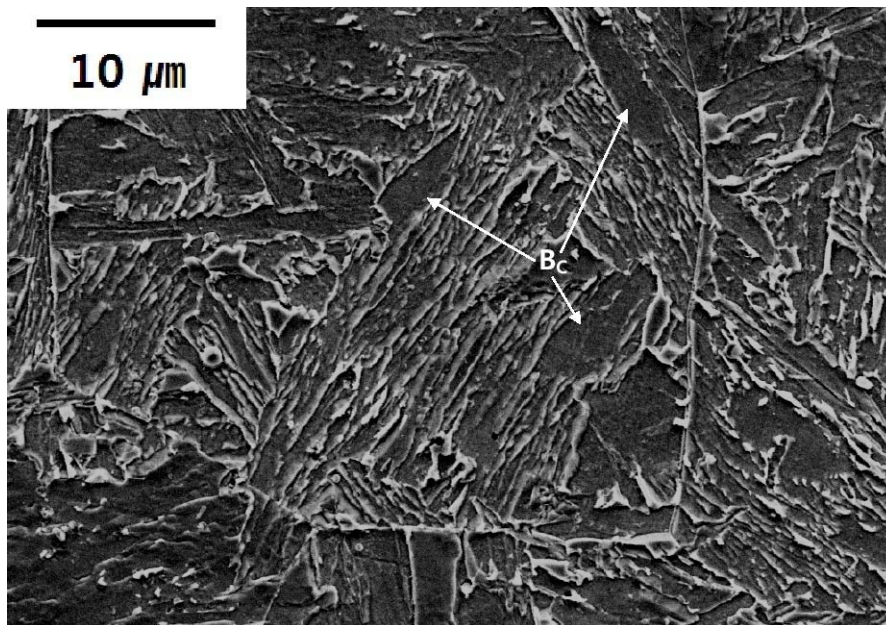
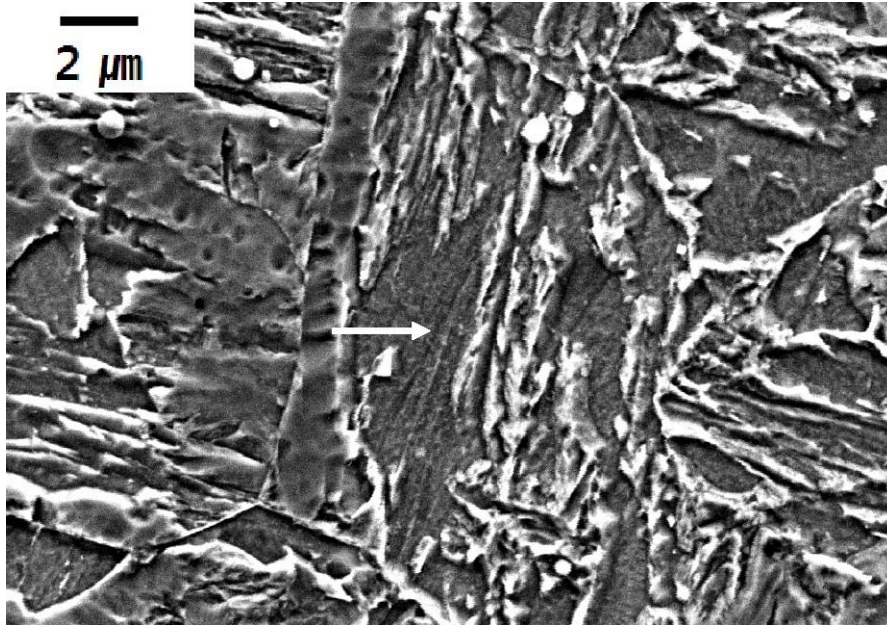


Fig. 5.11: Coalesced bainite in a sample transformed isothermally at 400 °C in the 0.5Mn alloy.

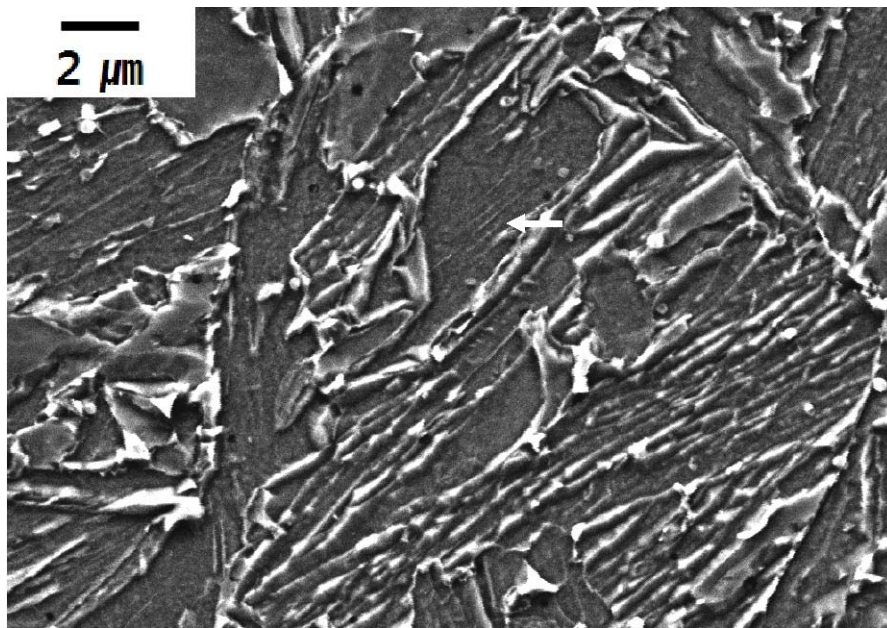
Fig. 5.11 is the FEGSEM micrograph of the sample which was isothermally transformed at 400 °C, showing coalesced bainite. Unfortunately the extent of coalescence could not be compared with that of the 2Mn alloy because there is no curve in the latter case which has a comparable maximum length change.

2.3 Uncertain constituents

Fig. 5.12 shows some constituents which were difficult to unambiguously classify. The morphology looks like that of coalesced bainite; however, there is structure within the apparently coarse grain in the form of finely separated lines, identified by an arrow in Fig. 5.12. The features have not yet been identified. The regions between the traces are about 0.2 micrometers in thickness, so it is conceivable that there are the component plates of a coalesced structure. This is reasonable for the transformation temperature (360 °C in the 2Mn alloy and 380 °C in the 0.5Mn alloy), so assuming that the traces do not correspond to austenite films, the coarser structure could be classified as coalesced bainite. After coalescence, there could be some low-misorientation boundaries left inside. However if the traces are thin austenite films, then the constituent should be classified as a packets of parallel bainite plates.



(a) 2Mn 360 °C



(b) 0.5Mn 380 °C

Fig. 5.12: Uncertain constituents those have internal traces.

3. Conclusions

Microscopy of samples isothermally transformed in the range between the bainite and martensite-start temperatures revealed the formation of coalesced bainite in reheated weld deposits. There seemed to be a greater tendency to form coalesced bainite at low temperatures, as expected from Chang and Bhadeshia's work (1996).

Coalesced bainite was observed not only at austenite grain surfaces but also occurred intragranularly. It has been confirmed that coalesced bainite occurs at the early stages of transformation.

Some constituents could not be unambiguously identified because although the overall appearance was consistent with that of coarse plates, there were fine parallel traces within the grain which could not be resolved. It will be necessary to conduct transmission electron microscopy to further characterise the detail.

VI. Summary and future work

The modelling of impact toughness for weld metal using a neural network method and the observation of coalesced bainite have been studied in detail.

In the modelling work, it was found that the logarithmic form of the output could cause an unjustified bias so the method was rejected. In subsequent predictions, it was discovered that increasing the interpass temperature can reduce the impact toughness when the former is below about 80 °C. Above that temperature the impact energy can increase as the interpass temperature is increased. There were interesting pattern of impact toughness in the plots of interpass temperature versus nickel which could be understood in terms of hardenability.

About coalesced bainite, there seemed to be a greater tendency to form coalesced bainite at low transformation temperatures. Coalesced bainite was observed not only at the austenite grain surfaces but also occurred intragranularly. It has been confirmed that as expected theoretically, coalesced bainite occurs at the early stages of transformation.

During this work, neural network modelling was focused on only impact toughness of weld metal. However, the other mechanical properties of weld metal, for example, yield strength, ultimate tensile strength or elongation are also challenging issues. Thus collecting data about them and creating many models for such mechanical properties should be continued. The ultimate aim is also to discover phenomena involving with the dramatic variation of such mechanical properties and to figure out their metallurgy.

For the work about coalesced bainite, the analyses using transmission electron microscope (TEM) and electron backscatter diffraction (EBSD) will be worthy for quantitative study for coalesced bainite. It will be especially

interesting to use confocal scanning laser microscopy (CSLM) to conduct real-time observations of the forming of coalesced bainite.

The study about the effect of coalesced bainite on mechanical properties is also important. The influence of not only the big size of the constituents but also the inhomogeneous distribution of their sizes is probably an interesting issue.

VII. References

Bhadeshia, H. K. D. H.: Neural networks in materials science, *ISIJ International*, Vol. 39 (1999a) No. 10 pp. 966-979

Bhadeshia, H. K. D. H.: Some phase transformations in steel, *Material Science and Technology*, Vol. (15) (1999b) pp. 22-29.

Bhadeshia, H. K. D. H.: *Bainite in steels*, IOM Communications Ltd, London, second edition, (2001)

Bhadeshia, H. K. D. H.: Frontiers in the modeling of steel weld deposits, *Journal of the Japan Welding Society*, Vol. 76 (2007) pp. 26-32

Bhadeshia, H. K. D. H. and Svensson, L. E.: Modelling the evolution of microstructure in steel weld metals. In Cerjak, H. and Easterling, K. E., editors, *Mathematical Modelling of Weld Phenomena*, The Institute of Materials, London, Vol. 1 (1993) pp. 109-182

Bhadeshia, H. K. D. H., Keehan, E., Karlsson, L. and Andrén, H.-O.: Coalesced bainite, *Transactions of the Indian Institute of Metals*, Vol. 59 (2006) pp. 689-694

Bhadeshia, H. K. D. H., Dimitriu, R., Pak, J. H. and Ryu, J. H.: On the performance of neural networks in materials science. submitted to *Materials Science and Technology*

Chang L. C., Bhadeshia H. K. D. H.: Microstructure of lower bainite formed at large undercoolings below bainite start temperature. *Materials Science and*

Technology, Vol. 12 (1996) pp. 233-236

Edvardson, T., Fredriksson, H. and Svensson, I.: A study of the solidification process of low carbon manganese steels, *Metal Science*, Vol. 6 (1976) pp. 297-306

Fujii, Hidetoshi, MacKay, D. J. C. and Bhadeshia, H. K. D. H.: Bayesian neural network analysis of fatigue crack growth rate in nickel base superalloys, *ISIJ International*, Vol. 36 (1996) pp. 1373-1382

Funderburk, Scott R.: Fundamentals of preheat, *Welding Innovation*, Vol. X IV, No. 2 (1997), pp. 14-15

Funderburk, Scott R.: The importance of interpass temperature, *Welding Innovation*, Vol. X V, No. 1 (1998), pp. 15-16

Funderburk, Scott R.: Postweld heat treatment, *Welding Innovation*, Vol. X V, No. 2 (1998), pp. 17-18

Funderburk, Scott R.: A look at heat input, *Welding Innovation*, Vol. X VI, No. 1 (1999), pp. 8-11

Keehan, E.: Effect of Microstructure on Mechanical Properties of High Strength Steel Weld Metals, Ph.D. thesis, Department of Experimental Physics, CHALMERS UNIVERSITY OF TECHNOLOGY AND GOTEBOURG UNIVERSITY (2004)

Keehan, E.: Microstructure and properties of novel high strength steel weld metals. *Welding in the World*, Vol. 49 (2005) pp. 19-31

Keehan, E., Karlsson, L., Andrén, H.-O., and Bhadeshia, H. K. D. H.: New development with C-Mn-Ni high strength steel weld metals, Part A – Microstructure, *Welding journal*, Vol. 85 (2006a) pp. 200-209

Keehan, E., Karlsson, L., Andrén, H.-O., and Bhadeshia, H. K. D. H.: New development with C-Mn-Ni high strength steel weld metals, Part B – Mechanical properties, *Welding journal*, Vol. 86 (2006b) pp. 218-224

Keehan, E., Karlsson, L., Thuvander, M. and Bergquist, E. L.: Microstructural characterization of as-deposited and reheated weld metal-High strength steel weld metal, IIW Doc. IX-2187-06

Kurz, W.: Mathematical Modelling of Weld Phenomena 2, editors. Cerjak, H. and Bhadeshia, H. K. D. H., London, *The Institute of Materials*, (1995) pp. 42

Lord, M.: Design and modelling of ultra - high strength steel weld deposits, Ph.D. Thesis, Materials Science and Metallurgy, University of Cambridge (1999)

MacKay David J. C.: A practical bayesian framework for backpropagation networks, *Neural Computation*, Vol. 4 (1992a) pp. 448-472

MacKay David J. C.: Bayesian interpolation, *Neural Computation*, Vol. 4 (1992b) pp. 415-447

MacKay David J. C.: Bayesian nonlinear modeling for the prediction competition, *ASHRAE Transactions: Symposia*, Vol. 100 (1994) pp. 1053-1062

MacKay David J. C.: Bayesian non-linear modelling with neural networks, Lecture notes for Cambridge course, *Modelling Phase Transformations in Steels*, (1995a) <http://www.inference.phy.cam.ac.uk/mackay/BayesNets.html>

MacKay David J. C.: Probable networks and plausible predictions – a review of practical bayesian methods for supervised neural networks, *Computation in Neural Systems*, Vol. 6 (1995b) pp. 469-505

Muruganath, M.: Design of welding alloys creep and toughness, Ph.D. thesis, Department of materials science and metallurgy, University of Cambridge (2002)

Ohkita, Shigeru, Horii, Yukihiro: Recent development in controlling the microstructure and properties of low alloy steel weld metals, *ISIJ International*, Vol. 35 (1995) pp. 1170-1182

Pickering, F. B.: Physical metallurgy and the design of steels, Materials science series, London, Applied science publishers, (1978)

Svensson, L. E.: Control of microstructure and properties in steel arc welds, CRC Press, Inc., (1994)

Svensson, L. E.: Consumables for welding high-strength steels, *Svetsaren*, Vol. 54 (1-2) (1999) pp. 29-33

Svensson, L. E., Gretoft, B. and Bhadeshia, H. K. D. H.: An analysis of cooling curves from the fusion zone of steel weld deposits, *Scandinavian Journal of Metallurgy*, Vol. 15 (1986) pp. 97-103

Wang, W. and Liu, S.; Alloying and microstructural management in

developing SMAW electrodes for HSLA-100 steel, *Welding Journal* , Vol. 81 (2002) pp. 132-145

Widgery, D. J., Karlsson, L., Muruganath, M. and Keehan, E.: Approaches to the development of high-strength weld metals, *Proceedings 2nd Int. Symposium on High-strength steel*, Stiklestad, Verdal, Norway: European Coal and Steel Community (ECBC), B-1049 Brussels, Belgium (2002)

Yang, Hong-Seok, Bhadeshia, H. K. D. H.: Uncertainties in dilatometric determination of martensite start temperature, *Materials Science and Technology*, Vol. 23 (2007) pp. 556-560

Yescas, M. A., Bhadeshia, H. K. D. H. and MacKay, D. J.: Estimation of the amount of retained austenite in austempered ductile irons using neural networks, *Materials Science and Engineering*, A311 (2001) pp. 162-173

Zhang, Z., Farrar, R. A.: Influence of Mn and Ni on the microstructure and toughness of C-Mn-Ni weld metals, *Welding journal*, Vol. 76 (1997) pp. 183-196

Literatures used for collecting data

Wang, W. and Liu S.: Alloying and microstructural management in developing SMAW electrodes for HSLA-100 steel, *Welding Journal*, Vol. 81 (2002) pp. 132-145

Ramini de Rissone, N. M., Farias, J. P., De Souza Bott, I. and Surian, E. S.: ANSI/AWS A5.1-91 E6013 rutile electrodes: The effect of calcite, *Welding Journal* , Vol. 81 (2002) pp. 113-124

Svoboda, H. G., Ramini de Rissone, N. M., De Vedia, L. A., and Surian, E. S.: The Effect of welding procedure on ANSI/AWS A5.29-98 E81T1-Ni1 Flux Cored Arc Weld Metal Deposits, *Welding Journal*, Vol. 83 (2004) pp. 301-307

Surian, E. S., Ramini de Rissone, N. M. and De Vedia, L. A.: Influence of molybdenum on ferritic high-strength SMAW all-weld-metal properties, *Welding Journal* , Vol. 84 (2005) pp. 53-62

Ramini de Rissone, N. M., Svoboda, H. G., Surian, E. S., and De Vedia, L. A.: Influence of procedure variables on C-Mn-Ni-Mo metal cored wire ferritic all-weld metal, *Welding Journal*, Vol. 84 (2005) pp. 139-148

Appendix A

Program MAP_STEEL_WELD_CHARPY

This appendix presents the model described in Chapter 4 and associated documentation following in MAP format.

<http://www.msm.cam.ac.uk/map/mapmain.html>.

1. Provenance of Source Code

Junhak Pak, March 2007, junhark@postech.ac.kr

Computational Metallurgy Laboratory,
Graduate Institute of Ferrous Technology,
POSTECH, Pohang, Korea.

The neural network program was produced by:

David MacKay,
Cavendish Laboratory, University of Cambridge,
Madingley Road, Cambridge, CB3 0HE, U.K.

2. Purpose

To estimate Charpy toughness of steel weld metal (manual metal arc, submerged arc, gas metal arc and gas tungsten arc), as a function of chemical composition, heat input, interpass temperature, post-weld heat treatment temperature and time, a variable for iron diffusion and test temperature.

3. Specification

Language: executables, C

Product form: executables

4. Description

A program which can be used for predicting Charpy toughness of weld metal (manual metal arc, submerged arc, gas metal arc and gas tungsten arc). The input variables required to run the program are chemical composition, heat input, interpass temperature, post-weld heat treatment temperature and time, a variable for iron diffusion and test temperature for Charpy test. The model is in fact a committee of nineteen models.

The downloadable package contains the following files and subdirectories (details may differ between LINUX and PC versions):

MINMAX

A text file containing the minimum and maximum limits of each input and output variable. This file is used to normalise and unnormalise the input and output data.

test.dat

An input text file containing the input variables used for predictions.

model.gen or model.exe

This is a unix shell file containing the command steps required to run the module. It can be executed by typing **cs** **model.gen** at the command prompt. This shell file compiles and runs all the programs necessary for normalising the input data, executing the network for each model, unnormalising the output data and combining the results of each model to produce the final *committee* result.

spec.t1

A dynamic file, created by **spec.ex**, which contains information about the module and the number of data items being supplied. It is read by the program **generate44**.

norm_test.in

This is a text file which contains the normalised input variables. It is generated by the program **normtest.for** in subdirectory **s**.

generate44

This is the executable file for the neural network program. It reads the normalised input data file, **norm_test.in**, and uses the weight files in subdirectory **c**. The results are written to the temporary output file **_out**.

_ot, _out, _res, _sen

These files are created by **generate44** and can be deleted.

Result

Contains the final un-normalised committee results for the predicted hardness.

SUBDIRECTOR Y s

spec.c

The source code for program **spec.ex**.

normtest.for

Program to normalise the data in **test.dat** and produce the normalised input file **norm_test.in**. It makes use of information read in from **no_of_rows.dat** and **committee.dat**.

gencom.for

This program uses the information in **committee.dat** and combines the predictions from the individual models, in subdirectory **outprdt**, to obtain an averaged value (*committee prediction*). The output (in normalised form) is written to **com.dat**.

treatout.for

Program to un-normalise the committee results in **com.dat** and write the output predictions to **unnorm_com**. This file is then renamed **Result**.

committee.dat

A text file containing the number of models to be used to form the committee result and the number of input variables. It is read by

gencom.for, **normtest.for** and **treatout.for**.

SUBDIRECTORY c

_w*f

The weights files for the different models.

***.lu**

Files containing information for calculating the size of the error bars for the different models.

_c*

Files containing information about the perceived significance value (MacKay, 1997) for each model.

_R*

Files containing values for the noise, test error and log predictive error (MacKay, 1997) for each model.

SUBDIRECTORY d

outran.x

A normalised output file which was created when developing the model. It is accessed by **generate44** via **spec.t1**.

SUBDIRECTORY outprdt

out1, out2 etc.

The normalised output files for each model.

com.dat

The normalised output file containing the committee results. It is generated by **gencom.for**.

Read me.text

Instructions for running the program.

5. References

1. MacKay, D.J.C.: Mathematical Modelling of Weld Phenomena 3, eds. Cerjak, H. and Bhadeshia, H.K.D.H., Inst. of Materials, London, pp 359 (1997)

6. Keywords

Neural network, steel, weld metal, Charpy, toughness

Acknowledgements

I am extremely grateful to my supervisor, Professor H. K. D. H. Bhadeshia. He showed me the simplicity and beauty of science and the fundamental attitude to be a researcher. And thanks to Professor Weijie Liu, Professor In Gee Kim and Professor Rongshan Qin for their advise, support and friendship.

I am also grateful to Dr. Leif Karlsson for the manufacture of the alloys and to Professor Bruno C. de Cooman for access to equipment. And also to Dr. Soran Biroscas, Seil Lee, Sun-Mi Shin, the staffs in TICM and the other Materials Design group members for helping with experiments and for discussions.

I would like to express my deep thanks to Hong-Seok Yang and Joo-Hyun Ryu. They never hesitated to discuss with me as co-workers even they were busy and helped me with experiments or dealing with computer software.

I also would like to express my thanks all the people including office staff in the Graduate Institute of Ferrous Technology (GIFT) in Pohang University of Science and Technology, especially those members in the Computational Metallurgy Laboratory (CML), for all their help and for all the happiness we shared. The life with CML members was quite pleasant and enjoyable.

I would like to thank Professor Hae-Geon Lee for introducing me to GIFT and for his kindness and encouragement when I joined GIFT. I acknowledge GIFT and POSCO for their financial support.

I also would like to thank Dr. Young-Jun Park, Seok-Jong Seo and Young-Ho Han. They kindly cared for me when I stayed in Cambridge.

Finally I would like to take this opportunity to express my gratitude to my family for their love, unfailing support. Especially my wife Sung-Hwa Seo encouraged me in Cambridge while I was writing my thesis. Since she stayed with me, I could complete this thesis.

CURRICULUM VITAE

Name: Pak, Jun Hak

Date of birth: 2 October 1980

Place of birth: Seoul, Republic of Korea

Address: Graduate Institute of Ferrous Technology, Pohang University of
Science and Technology San 31, Hyoja-Dong, Nam-gu, Pohang,
Kyungbuk, 790-784 Republic of Korea

Education:

M.S. 2008, POSTECH (Pohang, Korea), Graduate Institute of Ferrous
Technology, Computational Metallurgy.

B. S. 2006, YONSEI University (Seoul, Korea), Physics

Part of this work has been submitted to appear in the following publications:

Bhadeshia, H. K. D. H., Dimitriu, R., Pak, J. H. and Ryu, J. H.: On the
performance of neural networks in materials science, submitted to *Materials
Science and Technology*

Pak, Jun-Hak and Bhadeshia, H. K. D. H.: Neural network modelling of
impact toughness of weld metals, submitted to *Materials and Manufacturing
Processes*